Research Article

Integrated Guidance and Control Design of Rolling-Guided Projectile Based on Adaptive Fuzzy Control with Multiple Constraints

Shang Jiang, Fuqing Tian [ID], and Shiyan Sun

School of Weapons Engineering, Naval University of Engineering, 430033 Wuhan, China

Correspondence should be addressed to Fuqing Tian; tianfq001@126.com

In the terminal guidance section of large caliber naval gun-guided projectile while striking nearshore maneuvering target, an integrated guidance and control (IGC) method based on an adaptive fuzzy and block dynamic surface sliding mode (AFCBDSM) was proposed with multiple constraints, including the impact angle, control limitations, and limited measurement of the line of sight (LOS) angle rate. The strict feedback cascade model of rolling-guided projectile IGC in space was constructed, and the extended state observer (ESO) was used to estimate the LOS angle rate and uncertain disturbances inside and outside the system, such as target maneuvering, model errors, and wind. A nonsingular terminal sliding mode (NTSM) was designed to zero the LOS angle tracking errors and LOS angle rate in finite time, with the adaptive exponential reaching law. The cascade system was effectively stabilized by the block dynamic surface sliding mode, which prevented differential explosions. To compensate for the saturated nonlinearity of canard control constraints, an adaptive Nussbaum gain function was adopted. The switching chatter of the block dynamic surface sliding mode was reduced through adaptive fuzzy control. Proven by Lyapunov theory, the LOS angle tracking error and LOS angle rate were convergent in finite time, the closed-loop system was uniformly ultimately bounded (UUB), and the system states could be made arbitrarily small at the steady state. Hardware-in-the-loop simulation (HILS) experiments showed that the AFCBDSM provided the guided projectile with good guidance performance while striking targets with different maneuvering forms.

1. Introduction

In recent years, the rapid development of high-tech and advanced naval warfare theory has required naval gun weapons to be capable of continuous naval surface fire support and accurate striking of maritime and coastal targets. The naval gun-guided projectile, rolling at low speeds during flight, not only possesses a higher firing speed, more ammunition carrying capacity, and superior cost effectiveness than missiles, but it also has a longer range and higher accuracy compared with traditional ammunition, thereby providing reliable naval surface fire supports for amphibious forces [1].

Terminal guidance and control play a core role in achieving accurate strikes of naval gun-guided projectile. As attack and defense equipment systems are upgraded, the relative movement speed between the projectile and target increases, which makes the frequency of the guidance loop close to that of the control loop. Consequently, the frequency assumption of spectral separation might be invalid [2]. Due to the limited space of guided projectile control modules, it is necessary for guidance and control systems to share sensors, such as gyroscopes and accelerometers, to promote economic efficiency and reliability. Furthermore, to achieve a better damage effect, the multiple constraints of actual combat should be fully considered, such as the impact angle [3], nonlinear saturation of canard deflection [4], and limited measurements of the LOS angle rate [5]. The traditional time-scale separation design method that merely meets the miss-distance constraint has difficulty meeting the aforementioned requirements, which has attracted experts, scholars, and engineers to the IGC design method with multiple constraints.

IGC, first proposed by Williams et al. [6], utilizes the coupling relationship between the guidance and control system to construct a direct connection through aerodynamic angles and form a cascade closed-loop system. Based on the relative motion between the projectile and target, the control law of canard deflection can be directly calculated by IGC algorithm. Scholars have subsequently achieved results in IGC, combining it with robust control [7, 8], dynamic surface control [9, 10], adaptive control [7–9], sliding mode control (SMC) [11–14], fuzzy control [15], and other modern control theories. Yang et al. [7] proposed a robust IGC design method for guided projectile based on a SMC observer. Nevertheless, its high performance depended on precise measurements of the LOS angle rate, which was too demanding for rolling-guided projectile.

Backstepping control requires calculating high-order derivatives of virtual control laws, which easily leads to differential expansion. Therefore, Seyedipour et al. [9] designed a dynamic surface and adopted a low-pass filter to avoid differential expansion, which simplified the design process by guaranteeing the guidance performance and system stability. Combining it with ESO, Shao and Wang [10] designed a dynamic surface backstepping controller. The model error, target maneuvering, and other uncertain disturbances were observed by the ESO, which significantly reduced the switching range of the dynamic surface. The ESO, initially proposed by Han [16], is a feasible scheme to determine the time-varying nonlinear IGC problem with uncertain disturbances of which a simple algorithm can accurately observe the system states and internal and external disturbances without a precise model of the research object. As the sole actuator of the guided projectile, a canard usually exhibits deflection saturation phenomenon, which allows the available overload to be less than the required overload and easily leads to the system loss of control or even instability. Hence, Wen et al. [8] combined an adaptive Nussbaum gain function with the dynamic surface sliding mode, which effectively solved the nonlinear saturation of the actuator and stabilized the IGC cascade system.

Possessing strong robustness against instability factors, such as system parameter perturbations and external disturbances, SMC has been widely applied to the IGC design. Shtessel and Tournes [11] regarded the normal acceleration generated by target maneuver as a disturbance and designed the IGC method based on the high order sliding mode, which is robust against uncertainty disturbances of the target maneuver. To meet the terminal impact angle constraint, Wu and Yang [12] defined the impact angle as the angle between the projectile velocity and horizontal plane and proposed an effective IGC design scheme. However, it was pointed out that it is more universal to define the impact angle as the angle between the projectile velocity and target velocity at the moment of impact [13]. Furthermore, combining a block dynamic surface with ESO, an IGC method was proposed by Guo and Liang [14], which allowed the nonrolling near-space interceptor to obtain better guidance performance. It is well known that chatter is a difficult and urgent problem in SMC, which can be partially

improved by adopting a continuous saturation function. Resulting from the difficulty of determining switching gains, the effect of buffeting reduction must be further improved. Therefore, Ran et al. [15] designed an adaptive fuzzy system using the LOS angle rate and distance between the projectile and target, which not only effectively weakened chattering but it also improved the robustness of the whole system.

The previous research on IGC basically focused on nonrolling vehicles in a plane or space with a single constraint. However, there have been few IGC designs for rolling aircraft. A continuous roll character significantly enhances the couple relationship between the pitch and yaw channel of naval gun-guided projectiles, and multiple constraints introduce challenges to the finite-time convergence and stability of the system. With the above constraints and disturbances comprehensively considered in this paper, the AFCBDSM is proposed. It was proven using Lyapunov theory that the LOS angle tracking errors and LOS angle rate could converge in finite time, the closed-loop system was UUB, and the system states could be made arbitrarily small at the steady state. The main innovations were as follows: (1) with multiple constraints and various disturbances comprehensively considered, the IGC strict feedback cascade model for rolling naval gun-guided projectile was constructed, (2) the switching chatter of the block dynamic surface sliding mode was effectively weakened through adaptive fuzzy control, (3) the finite-time convergence of the LOS angle-tracking errors, LOS angle rate, and UUB of the closed-loop system were strictly proven, and (4) the effectiveness and feasibility of the AFCBDSM were verified by the designed HILS, which could satisfy multiple constraints.

2. Model Establishment

2.1. Motion and Mechanical Model. The relative motion relationship between the projectile and target in space is shown in Figure 1, where $Px_0y_0z_0$, $Px_2y_2z_2$, $Px_6y_6z_6$, $Tx_7y_7z_7$, and $Tx_8y_8z_8$ represent the projectile reference coordinate (N_P), projectile trajectory coordinate (P_V), LOS coordinate (Q_S), target reference coordinate (N_T), and target trajectory coordinate (T_V), respectively. Furthermore, P, T, R, θ_Q, and ψ_Q denote the projectile, target, distance between the projectile and target, LOS inclination angle, and LOS azimuth angle, respectively. θ_P, ψ_P, v_P, θ_T, ψ_T, and v_T denote the trajectory inclination angle, trajectory azimuth angle, and speed of the guided projectile and target, respectively.

In addition, θ, ψ, γ, α, β, δ_z, and δ_y represent the pitch angle, yaw angle, roll angle, attack angle, sideslip angle, pitch canard angle, and yaw canard angle, respectively. Because α, β, δ_z, and δ_y change periodically with the roll of the projectile, it is necessary to establish nonrolling coordinates [17], including quasi-projectile coordinates $Px_4y_4z_4$ and quasi-velocity coordinates $Px_5y_5z_5$. α^*, β^*, δ_{zeq}, and δ_{yeq} represent the quasi attack angle, quasi sideslip angle, equal pitch canard angle, and equal yaw canard angle, respectively, which are utilized to calculate forces and moments of the rolling-guided projectile. The transformation relations are given by
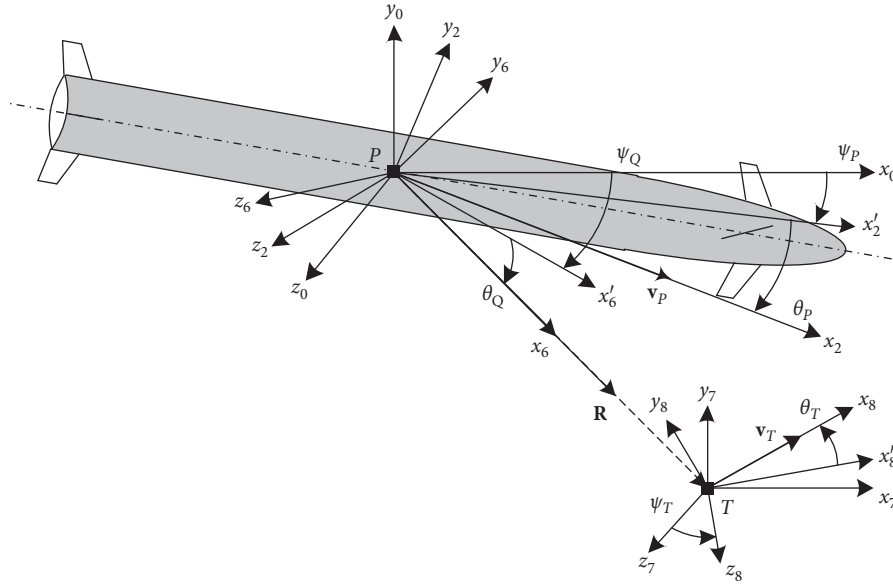
FIGURE 1: Relative motion relationship between the projectile and target in space.

$$\begin{bmatrix} \alpha^* \\ \beta^* \end{bmatrix} = \begin{bmatrix} \cos\gamma & \sin\gamma \\ -\sin\gamma & \cos\gamma \end{bmatrix} \begin{bmatrix} \alpha \\ \beta \end{bmatrix},$$

$$\begin{bmatrix} \delta_{zeq} \\ \delta_{yeq} \end{bmatrix} = \begin{bmatrix} \cos\gamma & \sin\gamma \\ -\sin\gamma & \cos\gamma \end{bmatrix} \begin{bmatrix} \delta_z \\ \delta_y \end{bmatrix}. \tag{1}$$

Assumption 1 (see [7]). The guided projectile can be regarded as a rigid body, and the target can be regarded as a particle. **R**, θ_Q, ψ_Q, θ_P, ψ_P, v_P, θ, ψ, and γ can be measured easily. P and T only possess acceleration in the normal direction of the respective velocity, which always satisfies $v_P > v_T$.

The transformation matrix from $Px_2y_2z_2$ to $Px_6y_6z_6$ is as follows:

$$\mathbf{C}_{Q_SP_V} = \begin{bmatrix} \varsigma_{Q_SP_{V11}} & \varsigma_{Q_SP_{V12}} & \varsigma_{Q_SP_{V13}} \\ \varsigma_{Q_SP_{V21}} & \varsigma_{Q_SP_{V22}} & \varsigma_{Q_SP_{V23}} \\ \varsigma_{Q_SP_{V31}} & \varsigma_{Q_SP_{V32}} & \varsigma_{Q_SP_{V33}} \end{bmatrix}. \tag{2}$$

The relative motion relationship between the projectile and target [18] is given by

$$\begin{bmatrix} \ddot{\theta}_Q \\ \ddot{\psi}_Q \end{bmatrix} = \begin{bmatrix} -\dfrac{2\dot{R}}{R}\dot{\theta}_Q - \dot{\psi}_Q^2\sin\theta_Q\cos\theta_Q - \dfrac{a_{Py_6}}{R} + \underbrace{\dfrac{a_{Ty_6}}{R}}_{d_{\theta_T}} \\ \\ -\dfrac{2\dot{R}}{R}\dot{\psi}_Q + 2\dot{\psi}_Q\dot{\theta}_Q\tan\theta_Q + \dfrac{a_{Pz_6}}{r} \underbrace{-\dfrac{a_{Tz_6}}{r}}_{d_{\psi_T}} \end{bmatrix}, \tag{3}$$

where d_{θ_T} and d_{ψ_T} are unknown disturbances caused by the target maneuver and $[a_{Px_6}, a_{Py_6}, a_{Pz_6}]^T$ and $[a_{Tx_6}, a_{Ty_6}, a_{Tz_6}]^T$ are components of the projectile acceleration $\mathbf{a}_P$ and target

acceleration $\mathbf{a}_T$ in $Px_6y_6z_6$, respectively. r is the projection of R on the yaw plane. The components of $\mathbf{a}_P$ in $Px_2y_2z_2$ and the components of $\mathbf{a}_T$ in $Tx_8y_8z_8$ are defined as $[0, a_{Py_2}, a_{Pz_2}]^T$ and $[0, a_{Ty_8}, a_{Tz_8}]^T$, respectively. The transformation relation for $\mathbf{a}_P$ from $Px_2y_2z_2$ to $Px_6y_6z_6$ can be obtained as follows:

$$\begin{bmatrix} a_{Py_6} \\ a_{Pz_6} \end{bmatrix} = \begin{bmatrix} a_{Py_2} \\ a_{Pz_2} \end{bmatrix} + \begin{bmatrix} \dfrac{(\varsigma_{Q_SP_{V22}} - 1)a_{Py_2} + \varsigma_{Q_SP_{V23}}a_{Pz_2}}{d_{a_{Py}}} \\ \\ \dfrac{\varsigma_{Q_SP_{V32}}a_{Py_2} + (\varsigma_{Q_SP_{V33}} - 1)a_{Pz_2}}{d_{a_{Pz}}} \end{bmatrix}, \tag{4}$$

where $d_{a_{Py}}$ and $d_{a_{Pz}}$ are coordinate transformation errors. The combined external force $\mathbf{F}_P$ acting on the projectile mainly consists of a gravitational force $\mathbf{G}$, lift force $\mathbf{R}_y$, Magnus force $\mathbf{R}_z$, equal operating force $\mathbf{F}_{\delta eq}$, and wind force $\mathbf{F}_w$. The components of $\mathbf{F}_P$ in the Py_2 and Pz_2 axes are the normal force F_{Py_2} and lateral force F_{Pz_2}, respectively. The external moment $\mathbf{M}$ mainly consists of a static moment $\mathbf{M}_z$, equatorial damping moment $\mathbf{M}_{zz}$, Magnus moment $\mathbf{M}_y$, equal operating moment $\mathbf{M}_{\delta eq}$, and wind moment $\mathbf{M}_w$. The components of $\mathbf{M}$ in the Pz_4 and Py_4 axes are the pitch moment M_{z_4} and yaw moment M_{y_4}, respectively. Their formulas can be written as follows:

$$F_{Py_2} = \underbrace{-mg\cos\theta_P}_{G_{y_2}} + \underbrace{QSc_y'\alpha^*}_{R_{yy_2}} - \underbrace{\frac{QS\,d\dot{\gamma}c_z''}{v_P}\beta^*}_{R_{zy_2}} + \underbrace{QSc_y^{\delta_z}sat_m(\delta_{zeq})}_{F_{\delta eqy_2}}$$

$$+ \underbrace{QSc_y'(\Delta\alpha_x + \Delta\alpha_y) - \frac{QS\,d\dot{\gamma}c_z''}{v_P}\Delta\beta_z}_{F_{wy_2}} + d_{F_{Py_2}},$$

$$F_{P_{z_2}} = \underbrace{-QSc_y'\beta^*}_{R_{yz_2}} - \underbrace{\frac{QS\,d\dot{\gamma}c_z''}{v_P}\alpha^*}_{R_{zz_2}} - \underbrace{QSc_y^{\delta_z}sat_m\left(\delta_{yeq}\right)}_{F_{\delta eqz_2}}$$

$$\underbrace{-QSc_y'\Delta\beta_z - \frac{QS\,d\dot{\gamma}c_z''}{v_P}\left(\Delta\alpha_x + \Delta\alpha_y\right)}_{F_{wz_2}} + d_{F_{Pz_2}},$$

$$M_{z_4} = \underbrace{QSlm_z'\alpha^*}_{M_{zz_4}} - \underbrace{\frac{QSl\,dm_{zz}'}{v_P}\dot{\theta}}_{M_{zzz_4}} - \underbrace{\frac{QSl\,d\dot{\gamma}m_y''}{v_P}\beta^*}_{M_{yz_4}}$$

$$+ \underbrace{QSl_c c_y^{\delta_z}sat_m\left(\delta_{zeq}\right)}_{M_{\delta eqz_4}}$$

$$+ \underbrace{QSlm_z'\left(\Delta\alpha_x + \Delta\alpha_y\right) - \frac{QSl\,d\dot{\gamma}m_y''}{v_P}\Delta\beta_z + d_{M_{z_4}}}_{M_{wz_4}},$$

$$M_{y_4} = \underbrace{QSlm_z'\beta^*}_{M_{zy_4}} - \underbrace{\frac{QSl\,dm_{zz}'\cos\theta}{v_P}\dot{\psi}}_{M_{zzy_4}} + \underbrace{\frac{QSl\,d\dot{\gamma}m_y''}{v_P}\alpha^*}_{M_{yy_4}}$$

$$+ \underbrace{QSl_c c_y^{\delta_z}sat_m\left(\delta_{zeq}\right)}_{M_{\delta eqy_4}}$$

$$+ \underbrace{QSlm_z'\Delta\beta_z + \frac{QSl\,d\dot{\gamma}m_y''}{v_P}\left(\Delta\alpha_x + \Delta\alpha_y\right) + d_{M_{y_4}}}_{M_{wy_4}},$$

$$\tag{5}$$

where $\dot{\theta}$ and $\dot{\psi}$ could be obtained through sensors of the projectile, such as microinertial navigation device and m, Q, S, d, l, and l_c are the mass, dynamic pressure, reference area, reference diameter, reference length, and distance from the canard to the pressure center of the guided projectile, respectively. c_y', c_z'', and $c_y^{\delta_z}$ represent the lift coefficient derivative, Magnus force coefficient joint partial derivative, and canard lift coefficient derivative, respectively. m_z', m_{zz}'', and m_y'' are the static moment coefficient derivative, equatorial damping moment coefficient derivative, and Magnus moment coefficient joint partial derivative, respectively. $d_{F_{Py_2}}$, $d_{F_{Pz_2}}$, $d_{M_{z_4}}$, and $d_{M_{Py_4}}$ represent unknown model errors of the force and moment. $\Delta\alpha_x$ and $\Delta\alpha_y$ are the additional attack angle caused by the vertical wind $\mathbf{w}_{x_0}$ and plumb wind $\mathbf{w}_{y_0}$,

respectively, and $\Delta\beta_z$ is the additional sideslip angle from the cross wind $\mathbf{w}_{z_0}$. These are related as follows:

$$\begin{cases} \Delta\alpha_x = -\arctan\left(\dfrac{\mathbf{w}_{x_0}\sin\theta_P}{\mathbf{v}_P}\right), \\[3mm] \Delta\alpha_y = \arctan\left(\dfrac{\mathbf{w}_{y_0}\cos\theta_P}{\mathbf{v}_P}\right), \\[3mm] \Delta\beta_z = -\arctan\left(\dfrac{\mathbf{w}_{z_0}\cos\psi_P}{\mathbf{v}_P}\right), \end{cases} \tag{6}$$

where $sat_m\left(\delta_{zeq}\right)$ is a continuous nondifferentiable saturation function defined as follows:

$$sat_m\left(\delta_{zeq}\right) = \begin{cases} \delta_{zeq}, & \left|\delta_{zeq}\right| \leq \delta_c^{\max}, \\[2mm] \delta_c^{\max}\mathrm{sign}\left(\delta_{zeq}\right), & \left|\delta_{zeq}\right| > \delta_c^{\max}, \end{cases} \tag{7}$$

where $\delta_c^{\max}$ is the maximum canard deflection angle and $sat_m\left(\delta_{yeq}\right)$ has the same form. For the convenience of the IGC design, the following reasonable assumption is made.

Assumption 2 (see [12]). $F_{P_{y_2}}$ and $F_{P_{z_2}}$ are mainly generated by α^* and β^*, respectively. The forces generated by δ_{zeq} and δ_{yeq} account for a small proportion of the lift force, which can be regarded as bounded uncertain disturbances.

The kinetics and kinematic equations of a projectile body rotating around mass center yield the following:

$$\ddot{\theta} = \frac{M_{z_4}}{J_{z_4}} + \underbrace{\frac{\left(J_{x_4} - J_{y_4}\right)}{J_{z_4}}\dot{\psi}^2\sin\theta\cos\theta}_{d_{M_{z_4}\dot{\psi}}} + \underbrace{\frac{J_{x_4}}{J_{z_4}}\dot{\psi}\dot{\gamma}\cos\theta}_{d_{M_{z_4}\dot{\gamma}}},$$

$$\ddot{\psi} = \frac{M_{y_4}}{J_{y_4}\cos\theta} + \underbrace{\frac{\left(J_{y_4} + J_{z_4} - J_{x_4}\right)}{J_{y_4}}\dot{\psi}\dot{\theta}\tan\theta}_{d_{M_{y_4}\dot{\theta}}} - \underbrace{\frac{J_{x_4}\dot{\theta}\dot{\gamma}}{J_{y_4}\cos\theta}}_{d_{M_{y_4}\dot{\gamma}}}. \tag{8}$$

Considering the delay characteristic of the canard as a first-order inertial link with time constant τ_c, the IGC model of a guided projectile can be obtained as follows:

$$\begin{bmatrix} \ddot{\theta}_Q \\ \ddot{\psi}_Q \end{bmatrix} = \underbrace{\begin{bmatrix} -\dfrac{2\dot{R}}{R}\dot{\theta}_Q - \dot{\psi}_Q^2\sin\theta_Q\cos\theta_Q + \dfrac{g\cos\theta_P}{R} \\[4mm] -\dfrac{2\dot{R}}{R}\dot{\psi}_Q + 2\dot{\psi}_Q\dot{\theta}_Q\tan\theta_Q \end{bmatrix}}_{f_2} + \underbrace{\begin{bmatrix} -\dfrac{QSc_y'}{mR} & 0 \\[4mm] 0 & -\dfrac{QSc_y'}{mr} \end{bmatrix}}_{a_2}\begin{bmatrix} \alpha^* \\ \beta^* \end{bmatrix} + \underbrace{\begin{bmatrix} -\dfrac{R_{zy_2} + F_{\delta y_2} + F_{wy_2} + d_{F_{Py_2}}}{mR} - \dfrac{d_{a_{Py}}}{R} + d_{\theta_T} \\[4mm] \dfrac{R_{zz_2} + F_{\delta z_2} + F_{wz_2} + d_{F_{Pz_2}}}{mr} - \dfrac{d_{a_{Pz}}}{r} + d_{\psi_T} \end{bmatrix}}_{d_2},$$

$$\begin{bmatrix} \dot{\alpha}^* \\ \dot{\beta}^* \end{bmatrix} = \underbrace{\begin{bmatrix} -\dfrac{QSc_y'}{mv_P}\alpha^* + \dfrac{QS\,d\dot{\gamma}c_z''}{mv_P^2}\beta^* + \dfrac{g\cos\theta_P}{v_P} \\[3mm] -\dfrac{QSc_y'}{mv_P\cos\theta_P}\beta^* - \dfrac{QS\,d\dot{\gamma}c_z''}{mv_P^2\cos\theta_P}\alpha^* \end{bmatrix}}_{f_3} + \underbrace{\begin{bmatrix} 1 & 0 \\ 0 & 1 \end{bmatrix}}_{a_3}\begin{bmatrix} \dot{\theta} \\ \dot{\psi} \end{bmatrix} + \underbrace{\begin{bmatrix} -\dfrac{F_{\delta y_2} + F_{wy_2} + d_{F_{Py_2}}}{mv_P} \\[3mm] \dfrac{F_{\delta z_2} + F_{wz_2} + d_{F_{Pz_2}}}{mv_P\cos\theta_P} \end{bmatrix}}_{d_3},$$

$$\begin{bmatrix} \ddot{\theta} \\ \ddot{\psi} \end{bmatrix} = \underbrace{\begin{bmatrix} \dfrac{QSlm_z'}{J_{z_4}}\alpha^* - \dfrac{QSl\,dm_{zz}'}{J_{z_4}v_P}\dot{\theta} - \dfrac{QSl\,d\dot{\gamma}m_y''}{J_{z_4}v_P}\beta^* + \dfrac{(J_{x_4} - J_{y_4})}{J_{z_4}}\dot{\psi}^2\sin\theta\cos\theta + \dfrac{J_{x_4}}{J_{z_4}}\dot{\psi}\dot{\gamma}\cos\theta \\[3mm] \dfrac{QSlm_z'}{J_{y_4}\cos\theta}\beta^* - \dfrac{QSl\,dm_{zz}'}{J_{y_4}v_P}\dot{\psi} + \dfrac{QSl\,d\dot{\gamma}m_y''}{J_{y_4}v_P\cos\theta}\alpha^* + \dfrac{(J_{y_4} + J_{z_4} - J_{x_4})}{J_{y_4}}\dot{\psi}\dot{\theta}\tan\theta - \dfrac{J_{x_4}\dot{\theta}\dot{\gamma}}{J_{y_4}\cos\theta} \end{bmatrix}}_{f_4}$$

$$+ \underbrace{\begin{bmatrix} \dfrac{QSl_c c_y^{\delta_z}}{J_{z_4}} & 0 \\[3mm] 0 & \dfrac{QSl_c c_y^{\delta_z}}{J_{y_4}\cos\theta} \end{bmatrix}}_{a_4}\begin{bmatrix} \mathrm{sat}_m(\delta_{zeq}) \\ \mathrm{sat}_m(\delta_{yeq}) \end{bmatrix} + \underbrace{\begin{bmatrix} \dfrac{M_{wz_4} + d_{Mz_4}}{J_{z_4}} \\[3mm] \dfrac{M_{wy_4} + d_{My_4}}{J_{y_4}\cos\theta} \end{bmatrix}}_{d_4},$$

$$\begin{bmatrix} \dot{\delta}_{zeq} \\ \dot{\delta}_{yeq} \end{bmatrix} = \underbrace{-\frac{1}{\tau_c}\begin{bmatrix} \delta_{zeq} \\ \delta_{zeq} \end{bmatrix}}_{f_5} + \underbrace{\frac{1}{\tau_c}\begin{bmatrix} 1 & 0 \\ 0 & 1 \end{bmatrix}}_{b}\begin{bmatrix} \delta_{zeq}^c \\ \delta_{yeq}^c \end{bmatrix} + \underbrace{\begin{bmatrix} d_{5_1} \\ d_{5_2} \end{bmatrix}}_{d_5}. \tag{9}$$

2.2. Nearshore Maneuvering Target Model.

A maritime and coastal maneuvering target can be approximately expressed by the following first-order term:

$$\begin{bmatrix} \dot{a}_{Ty_8} \\ \dot{a}_{Tz_8} \end{bmatrix} = \begin{bmatrix} \dfrac{(a_{Ty_8}^c - a_{Ty_8})}{\tau_{Ty_8}} \\[3mm] \dfrac{(a_{Tz_8}^c - a_{Tz_8})}{\tau_{Tz_8}} \end{bmatrix}, \tag{10}$$

where τ_{Ty_8} and τ_{Tz_8} are time constants and $a_{Ty_8}^c$ and $a_{Tz_8}^c$ are normal and lateral acceleration commands of the target, respectively, which are unknown and bounded.

2.3. Impact Angle Model.

In the pitch plane, the impact angle ϑ_E is defined as the angle between $\mathbf{v}_P$ and $\mathbf{v}_T$ at the final impact moment. Zeroing the relative normal velocity of the projectile and target leads to [3]

$$\theta_{Qf} = \theta_{Tf} - \arctan\left(\frac{\sin\vartheta_E}{v_T/v_P - \cos\vartheta_E}\right), \tag{11}$$

where θ_{Qf} and θ_{Tf} are the final LOS inclination angle and final target trajectory inclination angle, respectively, which can be acquired by unmanned reconnaissance. For any specified ϑ_E, there exists a unique θ_{Qf} corresponding to it, and the impact angle constraint can be converted into a LOS angle constraint.

2.4. System States Space.

The system state variables, input variables, and output variables are defined as follows:

$$\begin{aligned}
\mathbf{x}_1 &= \begin{bmatrix} \theta_Q - \theta_{Qf} \\ \psi_Q - \psi_{Qf} \end{bmatrix}, \\[2mm]
\mathbf{x}_2 &= \begin{bmatrix} \dot{\theta}_Q \\ \dot{\psi}_Q \end{bmatrix}, \\[2mm]
\mathbf{x}_3 &= \begin{bmatrix} \alpha^* \\ \beta^* \end{bmatrix}, \\[2mm]
\mathbf{x}_4 &= \begin{bmatrix} \dot{\theta} \\ \dot{\psi} \end{bmatrix}, \\[2mm]
\mathbf{x}_5 &= \begin{bmatrix} \delta_{zeq} \\ \delta_{yeq} \end{bmatrix}, \\[2mm]
u &= \begin{bmatrix} \delta_{zeq}^c \\ \delta_{zeq}^c \end{bmatrix}, \\[2mm]
\mathbf{y} &= \mathbf{x}_1.
\end{aligned} \tag{12}$$

For the convenience of the IGC design, a continuous differentiable hyperbolic tangent function vector $\mathbf{g}(\mathbf{x}_5)$ is introduced to describe the canard deflection saturation:

$$g(x_{5_j}) = \delta_c^{\max}\frac{\left(e^{x_{5_j}/\delta_c^{\max}} - e^{-x_{5_j}/\delta_c^{\max}}\right)}{\left(e^{x_{5_j}/\delta_c^{\max}} + e^{-x_{5_j}/\delta_c^{\max}}\right)}, \quad j = 1, 2. \tag{13}$$

The derivative function vector of $\mathbf{g}(\mathbf{x}_5)$ is $\dot{\mathbf{g}}(\mathbf{x}_5) = [\dot{g}(x_{5_1}), \dot{g}(x_{5_2})]^{\mathrm{T}}$ and

$$\dot{g}\left(x_{5_j}\right) = \frac{4}{\left(e^{x_{5_j}/\delta_c^{\max}} + e^{-x_{5_j}/\delta_c^{\max}}\right)^2}. \tag{14}$$

Moreover, the IGC strict feedback state space of a continuous rolling-guided projectile can be obtained as follows:

$$\begin{cases} \dot{\mathbf{x}}_1 = \mathbf{a}_1 \mathbf{x}_2, \\ \dot{\mathbf{x}}_2 = \mathbf{f}_2 + \mathbf{a}_2 \mathbf{x}_3 + \mathbf{d}_2, \\ \dot{\mathbf{x}}_3 = \mathbf{f}_3 + \mathbf{a}_3 \mathbf{x}_4 + \mathbf{d}_3, \\ \dot{\mathbf{x}}_4 = \mathbf{f}_4 + \mathbf{a}_4 \mathbf{g}(\mathbf{x}_5) + \mathbf{d}_4, \\ \dot{\mathbf{x}}_5 = \mathbf{f}_5 + \mathbf{b}\mathbf{u} + \mathbf{d}_5, \end{cases} \tag{15}$$
$$\mathbf{a}_1 = \begin{bmatrix} 1 & 0 \\ 0 & 1 \end{bmatrix},$$

where $\mathbf{d}_4 = \mathbf{d}_{40} + \mathbf{a}_4 [\text{sat}_m(\mathbf{x}_5) - \mathbf{g}(\mathbf{x}_5)]$. For the convenience of the IGC design, the following reasonable assumption is made.

Assumption 3 (see [13]). The disturbances d_{i_j} ($i = 2, 3, 4, 5$; $j = 1, 2$) and their first derivative are bounded, i.e., there are unknown normal numbers D_{i_j} and $\dot{D}_{i_j}$ that satisfy $|d_{i_j}| \le D_{i_j}$ and $|\dot{d}_{i_j}| \le \dot{D}_{i_j}$, respectively.

Remark 1. According to the definition of $\mathbf{d}_4$, one could be obtained that $\mathbf{d}_4$ is a continuous function in its definition domain and there is no discontinuous point. As result of the left derivative is not equal to the right derivative at $x_{5_j} = \pm\delta_c^{\max}$, and $\mathbf{d}_4$ is only nonderivative at $x_{5_j} = \pm\delta_c^{\max}$ in its definition domain. However, $\mathbf{d}_4$ is derivable in its definition domain except these two points, and the derivative is bounded.

3. AFCBDSM Design

The purpose of the AFCBDSM design is to generate an appropriate control law $\mathbf{u}$ for equation (14) that can allow $\mathbf{x}_1$ and $\mathbf{x}_2$ to converge to any small neighborhood of zero in finite time and guarantee the closed-loop system is UUB [19], and the system states converge to a small neighborhood of the origin, with limited measurements of $\mathbf{x}_2$, the control saturation of $\mathbf{x}_5$, and the unknown bounded disturbances $\mathbf{d}_i$.

3.1. ESO Design. To acquire an accurate observation value of $\mathbf{d}_2$, the following third-order ESO is designed, with the observational variables defined as $\mathbf{z}_{x_1} = [z_{x_{1_1}}, z_{x_{1_2}}]^{\mathrm{T}}$, $\mathbf{z}_{x_2} = [z_{x_{2_1}}, z_{x_{2_2}}]^{\mathrm{T}}$, and $\mathbf{z}_{d_2} = [z_{d_{2_1}}, z_{d_{2_2}}]^{\mathrm{T}}$:

$$\begin{cases} \mathbf{e}_{21} = \mathbf{z}_{x_1} - \mathbf{x}_1, \\ \mathbf{e}_{22} = \mathbf{z}_{x_2} - \mathbf{x}_2, \\ \mathbf{e}_{23} = \mathbf{z}_{d_2} - d_2, \\ \dot{\mathbf{z}}_{x_1} = \mathbf{z}_{x_2} - \boldsymbol{\beta}_{21}\mathbf{e}_{21}, \\ \dot{\mathbf{z}}_{x_2} = \mathbf{f}_2 + \mathbf{a}_2\mathbf{x}_3 + \mathbf{z}_{d_2} - \boldsymbol{\beta}_{22}\text{fal}(\mathbf{e}_{21}, \boldsymbol{\sigma}_{21}, \boldsymbol{\eta}_{21}), \\ \dot{\mathbf{z}}_{d_2} = -\boldsymbol{\beta}_{23}\text{fal}(\mathbf{e}_{21}, \boldsymbol{\sigma}_{22}, \boldsymbol{\eta}_{22}), \end{cases} \tag{16}$$

where $\boldsymbol{\beta}_{21} = \begin{bmatrix} \beta_{21_{11}} & 0 \\ 0 & \beta_{21_{22}} \end{bmatrix}$, $\boldsymbol{\sigma}_{21} = [\sigma_{21_1}, \sigma_{21_2}]^{\mathrm{T}}$, $\boldsymbol{\eta}_{21} = [\eta_{21_1}, \eta_{21_2}]^{\mathrm{T}}$, $\beta_{21_{jj}} > 0$, $0 < \sigma_{21_j} < 1$, $0 < \eta_{21_j} < 1$, and $\text{fal}(\mathbf{e}_{21}, \boldsymbol{\sigma}_{21}, \boldsymbol{\eta}_{21})$ is the function vector $[\text{fal}(e_{21_1}, \sigma_{21_1}, \eta_{21_1}), \text{fal}(e_{21_2}, \sigma_{21_2}, \eta_{21_2})]^{\mathrm{T}}$ [16].

In a previous report [3], the stability of the second- and third-order ESO designed in cascade systems were deduced and proven. By choosing appropriate parameters values, in particular, letting $\beta_{23_{jj}}$ be much larger than $\beta_{22_{jj}}$ and $\beta_{21_{jj}}$, the ESO given by equation (16) can observe $\mathbf{d}_2$ accurately and quickly. Similarly, for observing $\mathbf{d}_i$, the observational variables are defined as $\mathbf{z}_{x_i} = [z_{x_{i_1}}, z_{x_{i_2}}]^{\mathrm{T}}$ and $\mathbf{z}_{d_i} = [z_{d_{i_1}}, z_{d_{i_2}}]^{\mathrm{T}}$ and the second order ESO is designed as follows:

$$\begin{cases} \mathbf{e}_{i1} = \mathbf{z}_{x_i} - \mathbf{x}_i, \\ \mathbf{e}_{i2} = \mathbf{z}_{d_i} - \mathbf{d}_i, \\ \dot{\mathbf{z}}_{x_3} = \mathbf{f}_3 + \mathbf{a}_3\mathbf{x}_4 + \mathbf{z}_{d_3} - \boldsymbol{\beta}_{31}\mathbf{e}_{31}, \\ \dot{\mathbf{z}}_{x_4} = \mathbf{f}_4 + \mathbf{a}_4\mathbf{g} + \mathbf{z}_{d_4} - \boldsymbol{\beta}_{41}\mathbf{e}_{41}, \\ \dot{\mathbf{z}}_{x_5} = \mathbf{f}_5 + \mathbf{b}\mathbf{u} + \mathbf{z}_{d_5} - \boldsymbol{\beta}_{51}\mathbf{e}_{51}, \\ \dot{\mathbf{z}}_{d_i} = -\boldsymbol{\beta}_{i2}\text{fal}(\mathbf{e}_{i1}, \boldsymbol{\sigma}_i, \boldsymbol{\eta}_i), \end{cases} \tag{17}$$
$$i = 3, 4, 5.$$

3.2. Nonsingular Terminal Sliding Mode Design.

Lemma 1 (see [14]). *Considering the following system:*

$$\dot{\mathbf{x}} = f(\mathbf{x}, t),$$
$$f(\mathbf{0}, t) = 0, \tag{18}$$
$$x \in \mathbf{R}^n,$$

where $\mathbf{x} \in \mathbf{R}^n$ *is the system state vector,* $g(\mathbf{x}, t)$: $U_0 \times \mathbf{R} \longrightarrow \mathbf{R}^n$ *is a nonlinear continuous function defined on* $U_0 \times \mathbf{R}$, *and* $U_0 \in \mathbf{R}^n$ *is an open neighborhood of the origin* $\mathbf{x}(t) = 0$. *Assuming* $V(\mathbf{x})$ *is a* C^1 *smooth positive definite function defined on* $U \in \mathbf{R}^n$ *and* $\dot{V}(\mathbf{x}) + CV^A(\mathbf{x})$ *is negative semidefinite on* $U \in \mathbf{R}^n$ *for* $C \in \mathbf{R}^+$ *and* $A \in (0, 1)$, *there exists an area* U_0 *such that any* $V(\mathbf{x})$ *that starts from* $U_0 \in \mathbf{R}^n$ *can reach* $V(\mathbf{x}) \equiv 0$ *in finite time. Furthermore, if* T_r *is the time needed to reach* $V(\mathbf{x}) \equiv 0$, *then* $T_r \le V^{1-A}(\mathbf{x}_0)/[C(1 - A)]$, *where* $V(\mathbf{x}_0)$ *is the initial value of* $V(\mathbf{x})$.

A kind of NTSM is used to construct the sliding mode vectors:

$$\mathbf{s}_2 = \begin{bmatrix} s_{2_1} \\ s_{2_2} \end{bmatrix} = \mathbf{x}_1 + \begin{bmatrix} \mu_1|x_{2_1}|^{\delta_1}\text{sign}(x_{2_1}) \\ \mu_2|x_{2_2}|^{\delta_2}\text{sign}(x_{2_2}) \end{bmatrix}, \tag{19}$$

where $\mu_j > 0$ *and* $1 < \delta_j < 2$. *The time derivative of equation (19) can be obtained as follows:*

$$\dot{\mathbf{s}}_2 = \mathbf{x}_2 + \begin{bmatrix} \mu_1\delta_1|x_{2_1}|^{\delta_1-1} & 0 \\ 0 & \mu_2\delta_2|x_{2_2}|^{\delta_2-1} \end{bmatrix}[\mathbf{f}_2 + \mathbf{a}_2\mathbf{x}_3 + \mathbf{d}_2]. \tag{20}$$

To ensure good dynamic properties in the sliding mode approach process, the sliding mode adaptive approach law is designed as follows:

$$\dot{\mathbf{s}}_2 = -\mathbf{k}_2 \text{sign}(\mathbf{s}_2) - \frac{|\dot{R}|}{R}\mathbf{c}_2\mathbf{s}_2, \tag{21}$$

where $\mathbf{k}_2 = \begin{bmatrix} k_{2_{11}} & 0 \\ 0 & k_{2_{22}} \end{bmatrix}$, $|e_{21_i}| \le k_{2_{ii}}$, $\mathbf{c}_2 = \begin{bmatrix} c_{2_{11}} & 0 \\ 0 & c_{2_{22}} \end{bmatrix}$, $c_{2_{jj}} > 0$, *and* $\text{sign}(\mathbf{s}_2)$ *is a symbolic function vector* $[\text{sign}(s_{2_1}), \text{sign}(s_{2_2})]^T$. *Combining equations (20) and (21) and removing the singular factors* $|x_{2_1}|^{1-\delta_1}/\mu_1\delta_1$ *and* $|x_{2_2}|^{1-\delta_2}/\mu_2\delta_2$ *yields,*

$$\overline{\mathbf{x}}_3 = -\mathbf{a}_2^{-1}\left\{\left\{\begin{bmatrix} \dfrac{|x_{2_1}|^{2-\delta_1}\text{sign}(x_{2_1})}{\mu_1\delta_1} \\ \dfrac{|x_{2_2}|^{2-\delta_2}\text{sign}(x_{2_2})}{\mu_2\delta_2} \end{bmatrix} + \mathbf{f}_2 + \mathbf{z}_{d_2}\right. \right.$$

$$\left. + \mathbf{k}_2\text{sign}(\mathbf{s}_2) + \frac{|\dot{R}|}{R}\mathbf{c}_2\mathbf{s}_2\right\}. \tag{22}$$

Theorem 1. *For the subsystem composed of the first two equations of equation (15), adopting the ESO given by equation (16) and the control law given by equation (22), the system state variables* $\mathbf{x}_1$ *and* $\mathbf{x}_2$ *will converge to any small neighborhood of zero in finite time.*

Proof. A Lyapunov function is chosen as $V_2 = \mathbf{s}_2^{\text{T}}\mathbf{s}_2/2$, and the time derivative of V_2 can be obtained:

$$\dot{V}_2 = \mathbf{s}_2^{\text{T}}\dot{\mathbf{s}}_2 = \sum_{j=1}^{2} s_{2_j}\dot{s}_{2_j} = \sum_{j=1}^{2} s_{2_j}\left\{x_{2_j} + \mu_j\delta_j|x_{2_j}|^{\delta_j-1}\right.$$

$$\left[f_{2_j} + a_{2_{jj}}\overline{x}_{3_j} + d_{2_j}\right]\right\}$$

$$= \sum_{j=1}^{2} \mu_j\delta_j|x_{2_j}|^{\delta_j-1}s_{2_j}\left[d_{2_j} - z_{d_{2_j}} - k_{2_{jj}}\text{sign}(s_{2_j}) - \frac{|\dot{R}|}{R}c_{2_{jj}}s_{2_j}\right]$$

$$= -\sum_{j=1}^{2} \mu_j\delta_j|x_{2_j}|^{\delta_j-1}\left(\frac{|\dot{R}|}{R}c_{2_{jj}}s_{2_j}^2 - e_{21_j}s_{2_j} - k_{2_{jj}}|s_{2_j}|\right)$$

$$\le -\sum_{j=1}^{2}\left(k_{2_{jj}} - e_{21_j}\right)|s_{2_j}| \le -\min\left\{k_{2_{11}} - e_{21_1}, k_{2_{22}} - e_{21_2}\right\}$$

$$\cdot 2\sqrt{2}V_2^{1/2}. \tag{23}$$

According to Lemma 1, $\mathbf{s}_2$ can converge to **0** in finite time while $\mathbf{x}_2 \ne \mathbf{0}$, which is also satisfied if $\mathbf{x}_2 = \mathbf{0}$ [20]. Thus, the following can be obtained:

$$\dot{x}_{1_j} = -\mu_j^{-(1/\delta_j)}|x_{1_j}|^{1/\delta_j}\text{sign}(x_{1_j}). \tag{24}$$

A Lyapunov function is chosen as $V_{x_{1_j}} = x_{1_j}^2/2$, and the time derivative of $V_{x_{1_j}}$ can be obtained:

$$\dot{V}_{x_{1_j}} = -\mu_j^{-(1/\delta_j)}|x_{1_j}|^{(1/\delta_j)+1} = -2^{(1+\delta_j)/2\delta_j}\mu_j^{-(1/\delta_j)}V_{x_{1_j}}^{(1+\delta_j)/2\delta_j}. \tag{25}$$

According to Lemma 1, one can obtain $\mathbf{x}_1$, and $\mathbf{x}_2$ can converge to any small neighborhood of **0** in finite time. The proof ends. □

3.3. Block Dynamic Surface Sliding Mode Design. $\mathbf{s}_2$ is defined as the second block dynamic surface sliding mode, and the third, fourth, and fifth block dynamic surface sliding modes are defined as follows:

$$\begin{aligned}\mathbf{s}_3 &= \mathbf{x}_3 - \mathbf{x}_{3d}, \\ \mathbf{s}_4 &= \mathbf{x}_4 - \mathbf{x}_{4d}, \\ \mathbf{s}_5 &= \mathbf{g} - \mathbf{g}_d,\end{aligned} \tag{26}$$

where $\mathbf{g}$ is the abbreviated notation for the function $\mathbf{g}(\mathbf{x}_5)$. Virtual control laws $\overline{\mathbf{x}}_4$ and $\overline{\mathbf{g}}$ can be obtained [3] as follows:

$$\begin{cases} \overline{\mathbf{x}}_4 = -\left[\mathbf{f}_3 + \mathbf{z}_{d_3} - \dot{\mathbf{x}}_{3d} + \mathbf{k}_3\text{sign}(\mathbf{s}_3) + \mathbf{c}_3\mathbf{s}_3\right], \\ \overline{\mathbf{g}} = -\mathbf{a}_4^{-1}\left[\mathbf{f}_4 - \dot{\mathbf{x}}_{4d} + \mathbf{z}_{d_4} + \mathbf{k}_4\text{sign}(\mathbf{s}_4) + \mathbf{c}_4\mathbf{s}_4\right]. \end{cases} \tag{27}$$

To avoid direct differentiation with respect to $\overline{\mathbf{x}}_3$, $\overline{\mathbf{x}}_4$, and $\overline{\mathbf{g}}$, the filtered virtual control laws $\mathbf{x}_{3d}$, $\mathbf{x}_{4d}$, and $\mathbf{g}_d$ are obtained using the following first-order filter:

$$\begin{cases} \tau_3\dot{\mathbf{x}}_{3d} + \mathbf{x}_{3d} = \overline{\mathbf{x}}_3, & \mathbf{x}_{3d}(0) = \overline{\mathbf{x}}_3(0), \\ \tau_4\dot{\mathbf{x}}_{4d} + \mathbf{x}_{4d} = \overline{\mathbf{x}}_4, & \mathbf{x}_{4d}(0) = \overline{\mathbf{x}}_4(0), \\ \tau_5\dot{\mathbf{g}}_d + \mathbf{g}_d = \overline{\mathbf{g}}, & \mathbf{g}_d(0) = \overline{\mathbf{g}}(0), \end{cases} \tag{28}$$

where τ_3, τ_4, and τ_5 are positive constants.

Definition 1 (see [21]). If the continuous function $N(\chi)$ satisfies the following property $\lim_{t \to \infty}\sup (1/t)\int_0^t N(\chi)\text{d}\chi = \infty$ and $\lim_{t \to \infty}\sup (1/t)\int_0^t N(\chi)\text{d}\chi = -\infty$, then $N(\chi)$ is a Nussbaum function.

For handling the nonlinear saturation of the canard deflection effectively, control laws are designed as follows:

$$\begin{cases} \overline{\mathbf{u}} = -\dot{\mathbf{g}}\mathbf{f}_5 + \dot{\mathbf{g}}_d - \mathbf{k}_5\text{sign}(\mathbf{s}_5) - \mathbf{c}_5\mathbf{s}_5, \\ \mathbf{u} = \mathbf{b}^{-1}\left[\mathbf{N}(\chi)\overline{\mathbf{u}} - \mathbf{z}_{d5}\right], \end{cases} \tag{29}$$

where $\mathbf{k}_i$ and $\mathbf{c}_i$ ($i = 3, 4, 5$) are positive parameters whose form and scope are similar to $\mathbf{k}_2$ and $\mathbf{c}_2$, respectively. According to Definition 1, the following Nussbaum function is implemented:

$$\mathbf{N}(\boldsymbol{\chi}) = \begin{bmatrix} e^{\chi_1^2}\cos(\chi_1) & 0 \\ 0 & e^{\chi_2^2}\cos(\chi_2) \end{bmatrix}, \quad (30)$$

where χ_1 and χ_2 are adaptive variables of the Nussbaum function with the following adaptive law:

$$\dot{\boldsymbol{\chi}} = [\dot{\chi}_1, \dot{\chi}_2]^{\mathrm{T}} = \left[\gamma_{\chi_1}\overline{u}_1 s_{5_1}, \gamma_{\chi_2}\overline{u}_2 s_{5_2}\right]^{\mathrm{T}}, \quad (31)$$

where γ_{χ_1} and γ_{χ_2} are positive constants.

3.4. Adaptive Fuzzy System Design. Resulting from the time variability and nonlinearity of uncertain disturbances, it is difficult to determine appropriate switching gains, which causes serious chatter of the sliding mode. Possessing the universal approximation ability, the adaptive fuzzy system, composed of product inference, singleton fuzzification, center-average defuzzification, and Gauss membership functions [22], will be used to approximate observation error of disturbance. Thus, the high frequency chatter of the control law could be effectively weakened.

The input variable vector is defined as $\mathbf{w} = [w_1, \ldots, w_n]^{\mathrm{T}} \in \boldsymbol{\Omega}$, then there are $\prod_{j=1}^{n} p_j$ fuzzy rules in common as follows:

$$\text{Rule}^{(l_1,\ldots,l_n)}\text{: if } w_1 \text{ is } A_1^{l_1}, \ldots, w_n \text{ is } A_n^{l_n} \text{ then } \Xi(\mathbf{w}\,|\,\boldsymbol{\kappa}) \text{ is } B^{l_1,\ldots,l_n},$$
$$l_n = 1, \ldots, p_n, \quad (32)$$

where $\mathbf{A}_n^{l_n}$ are fuzzy sets associated with the fuzzy membership functions, and $\Xi(\mathbf{w}\,|\,\boldsymbol{\kappa})$ is the output variable as follows:

$$\Xi(\mathbf{w}\,|\,\boldsymbol{\kappa}) = \boldsymbol{\kappa}^{\mathrm{T}}\xi(\mathbf{w}) = \frac{\sum_{l_1=1}^{p_1}\cdots\sum_{l_n=1}^{p_n}\kappa^{l_1,\ldots,l_n}\prod_{i=1}^{n}\phi_{A_i^{l_i}}(w_i)}{\sum_{l_1=1}^{p_1}\cdots\sum_{l_n=1}^{p_n}\prod_{i=1}^{n}\phi_{A_i^{l_i}}(w_i)}, \quad (33)$$

where $\boldsymbol{\kappa} = [\kappa^{1,\ldots,1}, \ldots, \kappa^{p_1,\ldots,p_n}]^{\mathrm{T}}$ is an adaptive fuzzy parameter vector in the dimension of $\prod_{i=1}^{n} p_i$, $\phi_{A_n^{l_n}}(w_n)$ is the Gauss membership function, $\xi(\mathbf{w}) = [\xi^{1,\ldots,1}(\mathbf{w}), \ldots, \xi^{p_1,\ldots,p_n}(\mathbf{w})]^{\mathrm{T}}$ is the fuzzy basis vector in the dimension of $\prod_{i=1}^{n} p_i$, and the element is as follows:

$$\xi^{l_1,\ldots,l_n}(\mathbf{w}) = \frac{\prod_{i=1}^{n}\phi_{A_i^{l_i}}(w_i)}{\sum_{l_1=1}^{p_1}\cdots\sum_{l_n=1}^{p_n}\prod_{i=1}^{n}\phi_{A_i^{l_i}}(w_i)}. \quad (34)$$

Lemma 2 ([see 22]). *For a continuous function Γ defined in a closed set $\boldsymbol{\Omega} \subseteq \mathbf{R}^n$ and any precision ε, there must exist an adaptive fuzzy system $\Xi(\mathbf{w}\,|\,\boldsymbol{\kappa})$ composed of equations (33) and (34) such that it satisfies $\sup_{\mathbf{w}\in\boldsymbol{\Omega}} |\Gamma - \Xi(\mathbf{w}\,|\,\boldsymbol{\kappa})| \leq \varepsilon$.*

To guarantee the finite time convergence of $\mathbf{x}_1$ and $\mathbf{x}_2$, the adaptive fuzzy systems are designed for the virtual control law given by equation (27) and the control law given by equation

(29). *The optimal adaptive fuzzy parameter approximation vectors are defined as follows:*

$$\boldsymbol{\kappa}_{i_j}^* = \arg\min\left[\sup_{\mathbf{w}_{i_j}\in\boldsymbol{\Omega}}\left|-e_{i2_j} - \boldsymbol{\kappa}_{i_j}^{\mathrm{T}}\xi_{i_j}(\mathbf{w}_{i_j})\right|\right],$$
$$\boldsymbol{\kappa}_{5_j}^* = \arg\min\left[\sup_{\mathbf{w}_{5_j}\in\boldsymbol{\Omega}}\left|-\dot{g}_{jj}e_{52_j} - \boldsymbol{\kappa}_{5_j}^{\mathrm{T}}\xi_{5_j}(\mathbf{w}_{5_j})\right|\right], \quad (35)$$

where $\mathbf{w}_{i_j} = [s_{i_j}, \dot{s}_{i_j}]^{\mathrm{T}}$ $(i = 3, 4, 5)$. *According to Lemma 2, the following inequalities hold for any given small constant ε_{i_j}:*

$$\sup_{\mathbf{w}_{i_j}\in\boldsymbol{\Omega}}\left|-e_{i2_j} - \boldsymbol{\kappa}_{i_j}^{*\mathrm{T}}\xi_{i_j}(\mathbf{w}_{i_j})\right| \leq \varepsilon_{i_j}, \quad i = 3, 4; \ j = 1, 2,$$
$$\sup_{\mathbf{w}_{5_j}\in\boldsymbol{\Omega}}\left|-\dot{g}_{jj}e_{52_j} - \boldsymbol{\kappa}_{5_j}^{*\mathrm{T}}\xi_{5_j}(\mathbf{w}_{5_j})\right| \leq \varepsilon_{5_j}, \quad j = 1, 2. \quad (36)$$

The approximation errors of the fuzzy adaptive parameter vectors were defined as $\widetilde{\boldsymbol{\kappa}}_{i_j} = \boldsymbol{\kappa}_{i_j}^* - \boldsymbol{\kappa}_{i_j}$, of which the adaptive approach laws are as follows:

$$\dot{\boldsymbol{\kappa}}_{i_j} = \lambda_{i_j}\xi_{i_j}(\mathbf{w}_{i_j})s_{i_j} - \boldsymbol{\kappa}_{i_j}, \quad i = 3, 4, 5; \ j = 1, 2, \quad (37)$$

where $\lambda_{i_j} > 0$. *From equations (27) and (29), the virtual control laws and control law are, respectively, modified as follows:*

$$\begin{cases} \overline{\mathbf{x}}_4 = -\left[\mathbf{f}_3 + \mathbf{z}_{d_3} - \dot{\mathbf{x}}_{3d} + \Xi_3(\mathbf{w}_3\,|\,\boldsymbol{\kappa}_3) + \mathbf{c}_3\mathbf{s}_3\right], \\ \overline{\mathbf{g}} = -\mathbf{a}_4^{-1}\left[\mathbf{f}_4 - \dot{\mathbf{x}}_{4d} + \mathbf{z}_{d_4} + \Xi_4(\mathbf{w}_4\,|\,\boldsymbol{\kappa}_4) + \mathbf{c}_4\mathbf{s}_4\right], \\ \overline{\mathbf{u}} = -\dot{\mathbf{g}}\mathbf{f}_5 + \dot{\mathbf{g}}_d - \Xi_5(\mathbf{w}_5\,|\,\boldsymbol{\kappa}_5) - \mathbf{c}_5\mathbf{s}_5, \end{cases} \quad (38)$$

where $\Xi_i(\mathbf{w}_i\,|\,\boldsymbol{\kappa}_i) = [\Xi_{i_1}(\mathbf{w}_{i_1}\,|\,\boldsymbol{\kappa}_{i_1}), \Xi_{i_2}(\mathbf{w}_{i_2}\,|\,\boldsymbol{\kappa}_{i_2})]^{\mathrm{T}}$.

4. System Stability Analysis

Lemma 3 ([see 23]). *Let $V(t)$ and $\chi(t)$ be smooth functions, which are defined on $[0, t_f]$ with $V(t) \geq 0$. $\forall t \in [0, t_f)$, and $N(\cdot)$ is a Nussbaum gain function. If the following inequality holds, then $V(t)$ and $\chi(t)$ must be bounded on $[0, t_f]$:*

$$V(t) \leq V(0)e^{-Ct} + \frac{M}{C}\left(1 - e^{-Ct}\right) + \frac{e^{-Ct}}{\gamma_\chi}\int_0^t \dot{\chi}[\xi N(\chi) - 1]e^{C\tau}d\tau, \quad (39)$$

where $C > 0$ and $M > 0$. *The errors of the virtual control laws are defined as follows:*

$$\begin{aligned} \mathbf{y}_i &= \mathbf{x}_{id} - \overline{\mathbf{x}}_i, \\ \mathbf{Y}_g &= \mathbf{g}_d - \overline{\mathbf{g}}, \end{aligned} \quad (40)$$
$$i = 3, 4.$$

Differentiating $\mathbf{x}_{id}$ and $\mathbf{g}_d$ yields

$$\dot{\mathbf{x}}_{id} = -\frac{\mathbf{y}_i}{\tau_i}, \tag{41}$$

$$\dot{\mathbf{g}}_d = -\frac{\mathbf{y}_g}{\tau_5}.$$

Through some simple simplifications, we obtain the following:

$$\dot{\mathbf{y}}_i = \frac{-\mathbf{y}_i}{\tau_i} - \overline{\mathbf{x}}_i, \tag{42}$$

$$\dot{\mathbf{y}}_g = \frac{-\mathbf{y}_g}{\tau_5} - \overline{\mathbf{g}}.$$

According to a previous report [24], there are positive real numbers M_{i_j} and M_{g_j} such that the inequalities $\dot{\overline{x}}_{i_j} \le M_{i_j}$ and $\dot{\overline{g}}_j \le M_{g_j}$ hold. Through some simple calculations, we obtain

$$\mathbf{x}_i = \mathbf{s}_i + \mathbf{y}_i + \overline{\mathbf{x}}_i, \tag{43}$$

$$\mathbf{g} = \mathbf{s}_5 + \mathbf{y}_g + \overline{\mathbf{g}}.$$

We obtain the following Lyapunov function of the whole system state:

$$V = \frac{1}{2}\sum_{i=2}^{5}\mathbf{s}_i^{\mathrm{T}}\mathbf{s}_i + \frac{1}{2}\sum_{i=3}^{4}\mathbf{y}_i^{\mathrm{T}}\mathbf{y}_i + \frac{1}{2}\mathbf{y}_g^{\mathrm{T}}\mathbf{y}_g + \frac{1}{2}\sum_{j=1}^{2}\sum_{i=3}^{5}\frac{1}{\lambda_{i_j}}\widetilde{\boldsymbol{\kappa}}_{i_j}^{\mathrm{T}}\widetilde{\boldsymbol{\kappa}}_{i_j}. \tag{44}$$

Theorem 2. *For system (15), which satisfies Assumptions 1–3, the closed-loop system is UUB, and the system states could be made arbitrarily small at the steady state, with the application of the ESO given by equations (16) and (17), the block dynamic surface sliding mode given by equations (18) and (26), the control law given by equations (22) and (37), and the appropriate parameter selections.*

Proof. For convenience, taking the third dynamic surface s_{3_1} as an example, the simplification process of equalities and inequalities related to s_{3_1} is deduced as follows. From equations (27) and (28), one can obtain

$$s_{3_1}\dot{s}_{3_1} = s_{3_1}\left(\dot{x}_{3_1} - \dot{x}_{3d_1}\right)$$

$$= s_{3_1}\left[f_{3_1} + a_{3_{11}}\left(s_{4_1} + y_{4_1} + \overline{x}_{4_1}\right) + d_{3_1} - \dot{x}_{3d_1}\right]$$

$$= s_{3_1}\left(s_{4_1} + y_{4_1}\right) + s_{3_1}\left[d_{3_1} - z_{d3_1} - \boldsymbol{\kappa}_{3_1}^{\mathrm{T}}\xi_{3_1}\left(\mathbf{w}_{3_1}\right) - c_{3_1}s_{3_1}\right]$$

$$\le -\left(c_{3_1} - 1\right)s_{3_1}^2 + \frac{s_{4_1}^2}{2} + \frac{y_{4_1}^2}{2} + s_{3_1}\left[-e_{32_1} - \boldsymbol{\kappa}_{3_1}^{\mathrm{T}}\xi_{3_1}\left(\mathbf{w}_{3_1}\right)\right.$$

$$\left. + \boldsymbol{\kappa}_{3_1}^{*\mathrm{T}}\xi_{3_1}\left(\mathbf{w}_{3_1}\right) - \boldsymbol{\kappa}_{3_1}^{*\mathrm{T}}\xi_{3_1}\left(\mathbf{w}_{3_1}\right)\right]$$

$$\le -\left(c_{3_1} - 1\right)s_{3_1}^2 + \frac{s_{4_1}^2}{2} + \frac{y_{4_1}^2}{2} + \left|s_{3_1}\right|$$

$$\cdot \left|-e_{32_1} - \boldsymbol{\kappa}_{3_1}^{*\mathrm{T}}\xi_{3_1}\left(\mathbf{w}_{3_1}\right)\right| + s_{3_1}\widetilde{\boldsymbol{\kappa}}_{3_1}^{\mathrm{T}}\xi_{3_1}\left(\mathbf{w}_{3_1}\right)$$

$$\le -\left(c_{3_1} - \frac{3}{2}\right)s_{3_1}^2 + \frac{s_{4_1}^2}{2} + \frac{y_{4_1}^2}{2} + \frac{\varepsilon_{3_1}^2}{2} + \widetilde{\boldsymbol{\kappa}}_{3_1}^{\mathrm{T}}\xi_{3_1}\left(\mathbf{w}_{3_1}\right)s_{3_1}. \tag{45}$$

Differentiating $\widetilde{\boldsymbol{\kappa}}_{3_1}^{\mathrm{T}}\widetilde{\boldsymbol{\kappa}}_{3_1}/2\lambda_{3_1}$ yields

$$\frac{\widetilde{\boldsymbol{\kappa}}_{3_1}^{\mathrm{T}}\dot{\widetilde{\boldsymbol{\kappa}}}_{3_1}}{\lambda_{3_1}} = \frac{\widetilde{\boldsymbol{\kappa}}_{3_1}^{\mathrm{T}}\left[-\lambda_{3_1}\xi_{3_1}\left(\mathbf{w}_{3_1}\right)s_{3_1} + \boldsymbol{\kappa}_{3_1}\right]}{\lambda_{3_1}} = -\widetilde{\boldsymbol{\kappa}}_{3_1}^{\mathrm{T}}\xi_{3_1}\left(\mathbf{w}_{3_1}\right)s_{3_1} + \frac{\widetilde{\boldsymbol{\kappa}}_{3_1}^{\mathrm{T}}\left(\boldsymbol{\kappa}_{3_1}^* - \widetilde{\boldsymbol{\kappa}}_{3_1}\right)}{\lambda_{3_1}}$$

$$\le -\widetilde{\boldsymbol{\kappa}}_{3_1}^{\mathrm{T}}\xi_{3_1}\left(w_{3_1}\right)s_{3_1} - \frac{\widetilde{\boldsymbol{\kappa}}_{3_1}^{\mathrm{T}}\widetilde{\boldsymbol{\kappa}}_{3_1}}{2\lambda_{3_1}} + \frac{\boldsymbol{\kappa}_{3_1}^{*\mathrm{T}}\boldsymbol{\kappa}_{3_1}^*}{2\lambda_{3_1}}. \tag{46}$$

From equations (40) and (41), we have

$$y_{3_1}\dot{y}_{3_1} = y_{3_1}\left(-\dot{\overline{x}}_{3_1} - \frac{y_{3_1}}{\tau_3}\right) = -\frac{y_{3_1}^2}{\tau_3} - y_{3_1}\dot{\overline{x}}_{3_1}$$

$$\le -\frac{y_{3_1}^2}{\tau_3} + \frac{y_{3_1}^2 m_{3_1}^2}{\rho^2} + \frac{\rho^2}{4}. \tag{47}$$

Being similar to s_{3_1}, equalities and inequalities related to other dynamic surface could be obtained with no more detailed description. The derivative of equation (44) is as follows:

$$
\dot{V} = \sum_{j=1}^{2}\left(\sum_{i=2}^{5} s_{i_j}\dot{s}_{i_j} + \sum_{i=3}^{4} y_{i_j}\dot{y}_{i_j} + y_{g_j}\dot{y}_{g_j} + \sum_{i=3}^{5}\frac{1}{\lambda_{i_j}}\widetilde{\kappa}_{i_j}^{\mathrm{T}}\dot{\widetilde{\kappa}}_{i_j}\right)
$$

$$
= \sum_{j=1}^{2}\left[\!\!\left[s_{2_j}\left\{ x_{2_j} + \mu_j\delta_j\left|x_{2_j}\right|^{\delta_j-1}\left[f_{2_j} + a_{2_{jj}}\left(s_{3_j} + y_{3_j} + \bar{x}_{3_j}\right) + d_{2_j}\right]\right\} + s_{3_j}\left[f_{3_j} + a_{3_{jj}}\left(s_{4_j} + y_{4_j} + \bar{x}_{4_j}\right) + d_{3_j} - \dot{x}_{3d_j}\right] \right.\right.
$$

$$
+ s_{4_j}\left[f_{4_j} + a_{4_{jj}}\left(s_{5_j} + y_{g_j} + \bar{g}_j\right) + d_{4_j} - \dot{x}_{4d_j}\right] + s_{5_j}\left[\dot{g}_{jj}\left(f_{5_j} + b_j u_j + d_{5_j}\right) - \dot{g}_{d_j}\right] + \sum_{i=3}^{4} y_{i_j}\left(-\dot{\bar{x}}_{i_j} - \frac{y_{i_j}}{\tau_i}\right) + y_{g_j}\left(-\dot{g}_j - \frac{y_{g_j}}{\tau_5}\right)
$$

$$
\left.\left. - \sum_{i=3}^{5}\widetilde{\kappa}_{i_j}^{\mathrm{T}}\xi_{i_j}\left(\mathbf{w}_{i_j}\right)s_{i_j} + \sum_{i=3}^{5}\frac{1}{\lambda_{i_j}}\widetilde{\kappa}_{i_j}^{\mathrm{T}}\left(\kappa_{i_j}^{*} - \widetilde{\kappa}_{i_j}\right)\right]\!\!\right]
$$

$$
\leq \sum_{j=1}^{2}\left[\!\!\left[\mu_j\delta_j\left|x_{2_j}\right|^{\delta_j-1}a_{2_{jj}}s_{2_j}\left(s_{3_j} + y_{3_j}\right) + \mu_j\delta_j\left|x_{2_j}\right|^{\delta_j-1}s_{2_j}\left[d_{2_j} - z_{d2_j} - k_{2_{jj}}\mathrm{sign}\left(s_{2_j}\right) - \frac{|\dot{R}|}{R}c_{2_{jj}}s_{2_j}\right] + s_{3_j}\left(s_{4_j} + y_{4_j}\right)\right.\right.
$$

$$
+ s_{3_j}\left[d_{3_j} - z_{d3_j} - \kappa_{3_j}^{\mathrm{T}}\xi_{3_j}\left(\mathbf{w}_{3_j}\right) - c_{3_{jj}}s_{3_j}\right] + a_{4_{jj}}s_{4_j}\left(s_{5_j} + y_{g_j}\right) + s_{4_j}\left[d_{4_j} - z_{d4_j} - \kappa_{4_j}^{\mathrm{T}}\xi_{4_j}\left(\mathbf{w}_{4_j}\right) - c_{4_{jj}}s_{4_j}\right]
$$

$$
+ s_{5_j}\left\{\left[\dot{g}_{jj}N_{jj}(\chi_j) - 1\right]\bar{u}_j + \dot{g}_{jj}\left(d_{5_j} - z_{d5_j}\right) - \kappa_{5_j}^{\mathrm{T}}\xi_{5_j}\left(\mathbf{w}_{5_j}\right) - c_{5_{jj}}s_{5_j}\right\}
$$

$$
\left.\left. + \sum_{i=3}^{4} y_{i_j}\left(-\frac{y_{i_j}}{\tau_i} + M_{i_j}\right) + y_{g_j}\left(-\frac{y_{g_j}}{\tau_5} + M_{g_j}\right) - \sum_{i=3}^{5}\widetilde{\kappa}_{i_j}^{\mathrm{T}}\xi_{i_j}\left(\mathbf{w}_{i_j}\right)s_{i_j} - \frac{1}{2}\sum_{i=3}^{5}\frac{1}{\lambda_{i_j}}\widetilde{\kappa}_{i_j}^{\mathrm{T}}\widetilde{\kappa}_{i_j} + \frac{1}{2}\sum_{i=3}^{5}\frac{1}{\lambda_{i_j}}\kappa_{i_j}^{*\mathrm{T}}\kappa_{i_j}^{*}\right]\!\!\right]
$$

$$
\leq \sum_{j=1}^{2}\left[\!\!\left[\mu_j\delta_j\left|x_{2_j}\right|^{\delta_j-1}a_{2_{jj}}\left(s_{2_j}^2 + \frac{s_{3_j}^2}{2} + \frac{y_{3_j}^2}{2}\right) - \mu_j\delta_j\left|x_{2_j}\right|^{\delta_j-1}\frac{|\dot{R}|}{R}c_{2_{jj}}s_{2_j}^2 + \left(s_{3_j}^2 + \frac{s_{4_j}^2}{2} + \frac{y_{4_j}^2}{2}\right) - c_{3_{jj}}s_{3_j}^2 + \left(\frac{s_{3_j}^2}{2} + \frac{\varepsilon_{3_j}^2}{2}\right)\right.\right.
$$

$$
+ a_{4_{jj}}\left(s_{4_j}^2 + \frac{s_{5_j}^2}{2} + \frac{y_{g_j}^2}{2}\right) - c_{4_{jj}}s_{4_j}^2 + \left(\frac{s_{4_j}^2}{2} + \frac{\varepsilon_{4_j}^2}{2}\right) - c_{5_{jj}}s_{5_j}^2 + \left(\frac{s_{5_j}^2}{2} + \frac{\varepsilon_{5_j}^2}{2}\right) + s_{5_j}\left[\dot{g}_{jj}N_{jj}(\chi_j) - 1\right]\bar{u}_j
$$

$$
\left.\left. + \sum_{i=3}^{4}\left(\frac{M_{i_j}^2}{\rho^2} - \frac{1}{\tau_i}\right)y_{i_j}^2 + \left(\frac{M_{g_j}^2}{\rho^2} - \frac{1}{\tau_5}\right)y_{g_j}^2 - \frac{1}{2}\sum_{i=3}^{5}\frac{1}{\lambda_{i_j}}\widetilde{\kappa}_{i_j}^{\mathrm{T}}\widetilde{\kappa}i_j\right]\!\!\right] + \frac{3}{2}\rho^2 + \frac{1}{2}\sum_{j=1}^{2}\sum_{i=3}^{5}\frac{1}{\lambda_{i_j}}\kappa_{i_j}^{*\mathrm{T}}\kappa_{i_j}^{*}
$$

$$
\leq \sum_{j=1}^{2}\left[\!\!\left[\underbrace{-\mu_j\delta_j\left|x_{2_j}\right|^{\delta_j-1}\left(\frac{|\dot{R}|}{R}c_{2_{jj}} - a_{2_{jj}}\right)}_{m1}s_{2_j}^2 - \underbrace{\left(c_{3_{jj}} - \frac{\mu_j\delta_j\left|x_{2_j}\right|^{\delta_j-1}a_{2_{jj}}}{2} - \frac{3}{2}\right)}_{m2}s_{3_j}^2 - \underbrace{\left(c_{4_{jj}} - a_{4_{jj}} - 1\right)}_{m3}s_{4_j}^2\right.\right.
$$

$$
- \underbrace{\left(c_{5_{jj}} - \frac{a_{4_{jj}}}{2} - \frac{1}{2}\right)}_{m4}s_{5_j}^2 - \underbrace{\left(\frac{1}{\tau_3} - \frac{M_{3_j}^2}{\rho^2} - \frac{\mu_j\delta_j\left|x_{2_j}\right|^{\delta_j-1}a_{2_{jj}}}{2}\right)}_{m5}y_{3_j}^2 - \underbrace{\left(\frac{1}{\tau_4} - \frac{M_{4_j}^2}{\rho^2} - \frac{1}{2}\right)}_{m6}y_{4_j}^2 - \underbrace{\left(\frac{1}{\tau_5} - \frac{M_{g_j}^2}{\rho^2} - \frac{a_{4_{jj}}}{2}\right)}_{m7}y_{g_j}^2
$$

$$
\left.\left. - \underbrace{\frac{1}{2}\sum_{i=3}^{5}\frac{1}{\lambda_{i_j}}\widetilde{\kappa}_{i_j}^{\mathrm{T}}\widetilde{\kappa}_{i_j}}_{m8}\right]\!\!\right] + \sum_{j=1}^{2}\frac{\dot{\chi}_j}{\gamma_{\chi_j}}\left[\dot{g}_{jj}N_{jj}(\chi_j) - 1\right] + \underbrace{\frac{3}{2}\rho^2 + \frac{1}{2}\sum_{j=1}^{2}\sum_{i=3}^{5}\varepsilon_{i_j}^2 + \frac{1}{2}\sum_{j=1}^{2}\sum_{i=3}^{5}\frac{1}{\lambda_{i_j}}\kappa_{i_j}^{*\mathrm{T}}\kappa_{i_j}^{*}}_{\zeta}.
$$

$$
(48)
$$

The appropriate parameters are selected to meet the following requirements, which can guarantee the system stability:

$$\begin{cases} c_{2_{jj}} \geq \left(\ell + a_{2_{jj}}\right)\dfrac{R}{|\dot{R}|}, \\[2mm] c_{3_{jj}} \geq \ell + \mu_j \delta_j \left|x_{2_j}\right|^{\delta_j - 1} \dfrac{a_{2_{jj}}}{2} + \dfrac{3}{2}, \\[2mm] c_{4_{jj}} \geq \ell + a_{4_{jj}} + 1, \\[2mm] c_{5_{jj}} \geq \ell + \dfrac{a_{4_{jj}}}{2} + \dfrac{1}{2}, \\[2mm] \dfrac{1}{\tau_3} \geq \ell + \dfrac{m_{3_j}^2}{\rho^2} + \mu_j \delta_j \left|x_{2_j}\right|^{\delta_j - 1} \dfrac{a_{2_{jj}}}{2}, \\[2mm] \dfrac{1}{\tau_4} \geq \ell + \dfrac{m_{4_j}^2}{\rho^2} + \dfrac{1}{2}, \\[2mm] \dfrac{1}{\tau_5} \geq \ell + \dfrac{m_{g_j}^2}{\rho^2} + \dfrac{a_{4_{jj}}}{2}, \end{cases} \tag{49}$$

where ℓ is an arbitrary positive constant. Letting the positive constant $\varpi = \min\{m_i (i = 1, \ldots, 8)\}$, equation (48) can be simplified as follows:

$$\dot{V} \leq -2\varpi V + \zeta + \sum_{j=1}^{2} \frac{\dot{\chi}_j}{\gamma_{\chi_j}}\left[\dot{g}_{jj} N_{jj}(\chi_j) - 1\right]. \tag{50}$$

Suppose $\varpi > \left\{\zeta + \sum_{j=1}^{2}(\dot{\chi}_j/\gamma_{\chi_j})[\dot{g}_{jj}N_{jj}(\chi_j) - 1]\right\}/(2b)$, then it could be obtained that $\dot{V} < 0$ on $V = b$, which means that $V \leq b$ is an invariant set, and if $V(t_r) \leq b$, then $V(t) \leq b$ holds for all $t \geq t_r$. By the comparison principle [23], the following can be concluded from equation (50):

$$0 \leq V(t) \leq V(0)e^{-2\varpi t} + \frac{\zeta}{2\varpi}\left(1 - e^{-2\varpi t}\right)$$
$$+ e^{-2\varpi t}\sum_{j=1}^{2}\frac{1}{\gamma_{\chi_j}}\int_0^t \dot{\chi}_j\left[\dot{g}_{jj}N_{jj}(\chi_j) - 1\right]e^{2\varpi\tau}\mathrm{d}\tau. \tag{51}$$

According to Lemma 3, one could obtain that V is bounded by $\zeta/2\varpi$ and the closed-loop system is UUB. Furthermore, ζ is a constant independent of ϖ, so the upper bound $\zeta/2\varpi$ could be made arbitrarily small through tuning the design parameters, of which the purpose is for ζ small enough and ϖ big enough. Thus, the system states could be made arbitrarily small at the steady state. The proof ends. □

Similar to the existing literatures [25], Theorem 2 shows the existence of the control algorithm to ensure the stability of the closed-loop system but does not provide a quantitative criterion on how to select the design parameters. In fact, it is difficult to give such a criterion. By far, the design parameters can only be selected by trial and error.

5. Experimental Results and Discussions

To verify the effectiveness and feasibility of the AFCBDSM, the control module of a naval gun-guided projectile was selected as the control object and a HILS system was built, as shown in Figure 2, which mainly included a host computer, three-axis turntable, industrial personal computer (IPC), and control module, including a microcontrol unit (MCU) and dual channel canard. The main performance indexes of the canard and turntable are shown in Tables 1 and 2, respectively, which meet the requirements of the HILS.

The core component of the HILS system was the STM32F429IGT6 MCU, which configured the RS232 bus communication, interruption, direct memory access (DMA), and analog-to-digital converter (ADC) according to the program compiled in Keil. The host computer controlled the states of the hardware-in-the-loop simulation system by sending control instructions to the control module, such as the initial, start, stop, and recovery instructions. After starting the simulation, the MCU uses a Kalman filter to process the canard deflection feedback collected by the ADC in real time and obtained attitude feedback from the IPC. These feedback parameters and the fourth order Runge–Kutta method were used to iterate the differential equations with a 10 ms step, which was composed of six-degree-of-freedom equations of the projectile, three-degree-of-freedom equations of the target, the relative motion equations, the Kalman filter, and the AFCBDSM. The corresponding parameters were solved and sent back to the host computer. Meanwhile, the MCU sent the canard deflection and attitude commands to the dual channel canard and IPC, respectively. Based on the commands from the MCU, the canard drove its wings to deflect and the IPC drove the turntable to rotate. The simulation stopped until the distance between the projectile and target was less than the lethal radius. To ensure the efficient operation of the MCU and real-time communication between the devices, DMA was applied to the links with large amount of data.

The parameters of the projectile, the parameters of the motion and system, and the parameters of the guidance and control were shown in Tables 3–5, respectively. In order to reflect AFCBDSM, it does not need $\mathbf{x}_2$, $\mathbf{z}_{x_2}$ used in equations (22) and (37). In addition, the radius of the seeker blind area was set as 50 m, where the control law of the canard deflection was unchanged and the projectile relied on inertial flight. The initial values of the adaptive fuzzy system parameters vectors $\boldsymbol{\kappa}_{i_j}$ were $\mathbf{0}$, and the following Gauss fuzzy membership function was adopted:

$$\phi_{a_{i_j}^{l_{i_j}}}\left(s_{i_j}\right) = e^{-\left[10s_{i_j} + 1 - \left((l_{i_j} - 1)/2\right)\right]^2},$$
$$i = 3, 4, 5; j = 1, 2; l_{i_j} = 1, \ldots, 5,$$
$$\phi_{a_{i_j}^{l_{i_j}}}\left(\dot{s}_{i_j}\right) = e^{-\left[5\dot{s}_{i_j} + 2 - \left((l_{i_j} - 1)/2\right)\right]^2}, \tag{52}$$
$$i = 3, 4, 5; j = 1, 2; l_{i_j} = 1, \ldots, 9.$$
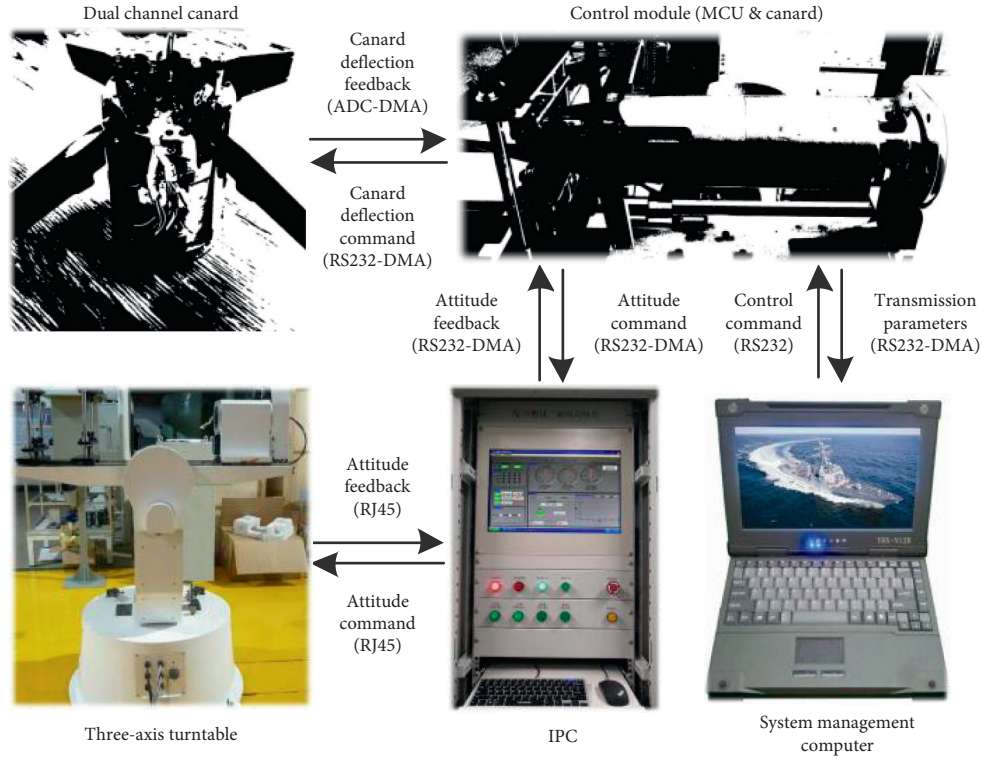
FIGURE 2: Hardware-in-the-loop simulation system.

TABLE 1: Main indexes of canard.

Index	Value
Output torque (N·m)	≥3
Max canard angle (deg)	±18
Response frequency (Hz)	≥6
Baud rate (bps)	115200
Max error of canard deflection (deg)	±0.1

TABLE 2: Main indexes of turntable.

Index	Value
Pitch angle (deg)	±80
Yaw angle (deg)	±40
Roll angle (deg)	Continuous
Angle accuracy (deg)	±0.1
Pitch rate (deg·s^{-1})	≥10
Yaw rate (deg·s^{-1})	≥10
Roll rate (deg·s^{-1})	≥3600
Overload mass (kg)	≤15

TABLE 3: Parameters of projectile.

Parameter	Value
m (kg)	43.500
l (m)	1.492
l_c (m)	0.217
d (m)	0.130
$\delta_c^{\max}$ (deg)	15
τ_c	0.1
c_y'	23.130
c_z''	0.337
$c_y^{\delta_z}$	4.925
m_z'	−7.035
m_{zz}'	11.444
m_y''	−0.337

$$\text{sat}(\cdot) = \frac{\cdot}{(|\cdot| + \delta)}, \quad \delta > 0, \tag{53}$$

where δ is a small positive constant.

To strike targets with sinusoidal and square wave maneuvers, the HILS and digital simulation of the AFCBDSM were carried out, respectively. For comparison, the adaptive dynamic surface control (ADSC) [23] and conventional guidance and control (G&C) design method [25] were simulated numerically under the same conditions. G&C used the PID controller and proportional navigation guidance (PNG) with navigation constant of 4. To reduce chatter of control law, ADSC used the following continuous saturation function instead of a symbolic function:

5.1. Operating Condition 1: Sinusoidal Maneuvering Target. The acceleration commands for a sinusoidal maneuvering target were set as follows:

$$a_{Ty_8}^c = 3\sin(t)\left(\text{m·s}^{-2}\right),$$
$$a_{Tz_8}^c = -3\sin(t)\left(\text{m·s}^{-2}\right). \tag{54}$$

The experimental results and curves are, respectively, shown in Figure 3 and Table 6, where AFCBDSM-D, AFCBDSM-H, ADSC-D, and G&C-D represent digital

Table 4: Parameters of motion and system.

Parameter	Value
Initial position of P (m)	$(0, 4000, 0)$
Initial position of T (m)	$(3000, 0, 300)$
Initial θ_P, ψ_P (deg)	$(-10, 0)$
Initial θ_T, ψ_T (deg)	$(0, 0)$
θ_{Qf}, ψ_{Qf} (deg)	$(-65, -10)$
$d_{F_{Py_2}}$, $d_{F_{Pz_2}}$ (N)	$5\sin(t)$
$d_{M_{Pz_4}}$, $d_{M_{Py_4}}$ (N·m)	$5\cos(t)$
d_{5_1}, d_{5_2} (deg·s^{-1})	$\sin(t)$
τ_{Ty_8}	0.01
τ_{Tz_8}	0.01
v_P (m·s^{-1})	357
v_T (m·s^{-1})	30
w_{x_0} (m·s^{-1})	5
w_{y_0} (m·s^{-1})	5
w_{z_0} (m·s^{-1})	5

Table 5: Parameters of guidance and control.

Item	Value
$\beta_{21_{11}}$	8
σ_{21_1}	0.02
δ_1	1.5
τ_3	0.01
$\beta_{21_{22}}$	8
σ_{21_2}	0.01
δ_2	1.7
τ_4	0.01
$\beta_{22_{11}}$	80
η_{21_1}	0.1
$k_{2_{11}}$	0.3
τ_5	0.01
$\beta_{22_{22}}$	80
η_{21_2}	0.025
$k_{2_{22}}$	0.5
λ_{3_1}	50
$\beta_{23_{11}}$	550
μ_1	12
$c_{2_{11}}$	3
λ_{3_2}	60
$\beta_{23_{22}}$	550
μ_2	15
$c_{2_{22}}$	5

simulations of AFCBDSM, HILS of AFCBDSM, digital simulation of ADSC, and digital simulation of G&C, respectively.

As shown in Figure 3(a), the trajectory of the projectile and target illustrated that AFCBDSM, ADSC, and G&C could both make the guided projectile hit the sinusoidal maneuvering target. As shown in Table 6, one can obtain that the trajectory of the AFCBDSM was flatter than ADSC and G&C, which further improved the miss distance, hit time, and LOS angle tracking errors. This showed that the adaptive fuzzy control effectively improved the terminal guidance performance. The change in the normal overload can be analyzed from Figure 3(b). Because ADSC only used a continuous saturation function with constant coefficients,

the chatter of the dynamic surface sliding mode was larger and the peak value and range of overload were significantly larger than that of the AFCBDSM, which made the variation of the control instructions smoother and converge near the end because of the adaptive fuzzy system and block dynamic surface, which is more in line with the actual operational needs.

As shown in Figure 3(c), the variation of α^* was basically consistent with normal overload, which verifies the rationality of Assumption 2. Significantly affected by the channel coupling and winds during the terminal guidance process, ADSC and G&C mutated in the initial stage and even diverged in the final stage, which was not conducive to stable flight. Nevertheless, under the joint control of the ESO and adaptive fuzzy systems, the AFCBDSM reduced the peak value and variation range of α^*.

As shown in Figure 3(d), by introducing the adaptive Nussbaum function, the AFCBDSM effectively handled the nonlinear saturation and protected canard better, so as to avoid failing to reach the tactical index due to canard deflection saturation.

Based on Figure 3(e), the pitch channel of the canard could meet requirements of the actual canard deflection in the switching frequency and amplitude. Resulting from the adaptive adjustment of fuzzy parameters, the AFCBDSM further ameliorated the range and mutation of δ_z, unlike ADSC and G&C.

The change of $\dot{\theta}_Q$ is shown in Figure 3(f). Under the control of the AFCBDSM, $\dot{\theta}_Q$ maintained a stable convergent state after 8 s, which not only indicated $\mathbf{x}_1$ and $\mathbf{x}_2$ were able to converge to zero in finite time, but also verified the correctness of the finite-time convergent property of $\mathbf{s}_2$ given in Theorem 1.

Figure 3(g) shows that the change in θ was smooth and continuous during the guidance process. It also illustrated that the pitch channel of turntable exhibited good servo performance. Under the control of adaptive fuzzy systems and block dynamic surface sliding modes, the AFCBDSM exhibited not only a faster convergence rate than ADSC and G&C, but also smaller overshoot.

Figures 3(f), 3(h), and 3(i) revealed the good observational properties and robustness of the designed ESO, which could quickly provide accurate observations of $\dot{\theta}_Q$ and uncertain disturbances for effectively hitting a sinusoidal maneuvering target. Additionally, it could reduce the hardware design requirement of the guided projectile.

5.2. Operating Condition 2: Square Wave Maneuvering Target. The acceleration commands of a square wave maneuvering target were set as follows:

$$a_{Ty_8}^c = 3\text{sign}[\sin(t)]\left(\text{m·s}^{-2}\right),$$
$$a_{Tz_8}^c = -3\text{sign}[\sin(t)]\left(\text{m·s}^{-2}\right). \tag{55}$$

The experimental results and curves were shown in Figure 4 and Table 7, respectively.

As shown in Figure 4(a), both the AFCBDSM, ADSC, and G&C could be utilized in the terminal guidance stage of

(a)

(b)

(c)

(d)

(e)
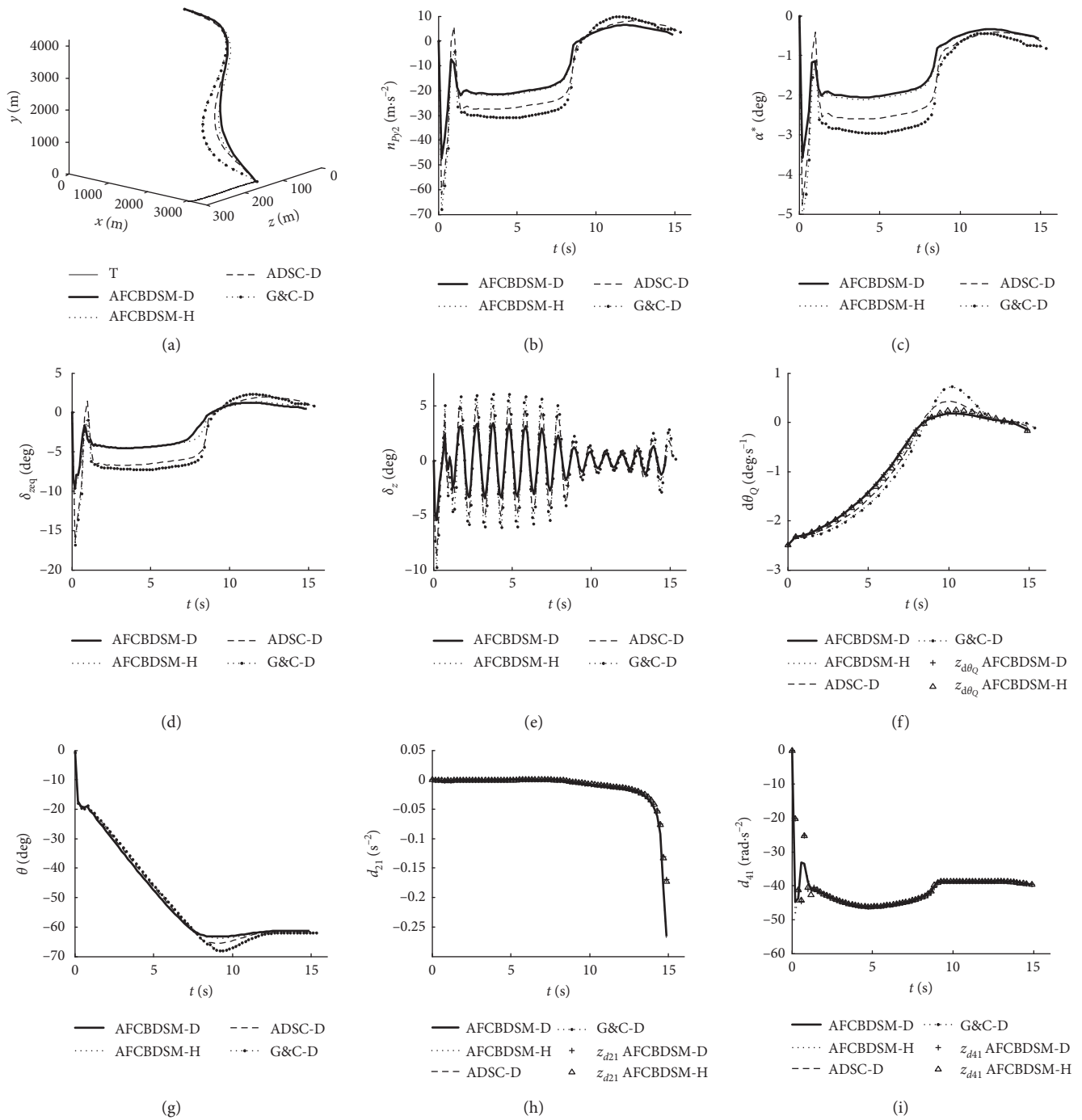

(f)

(g)

(h)

(i)
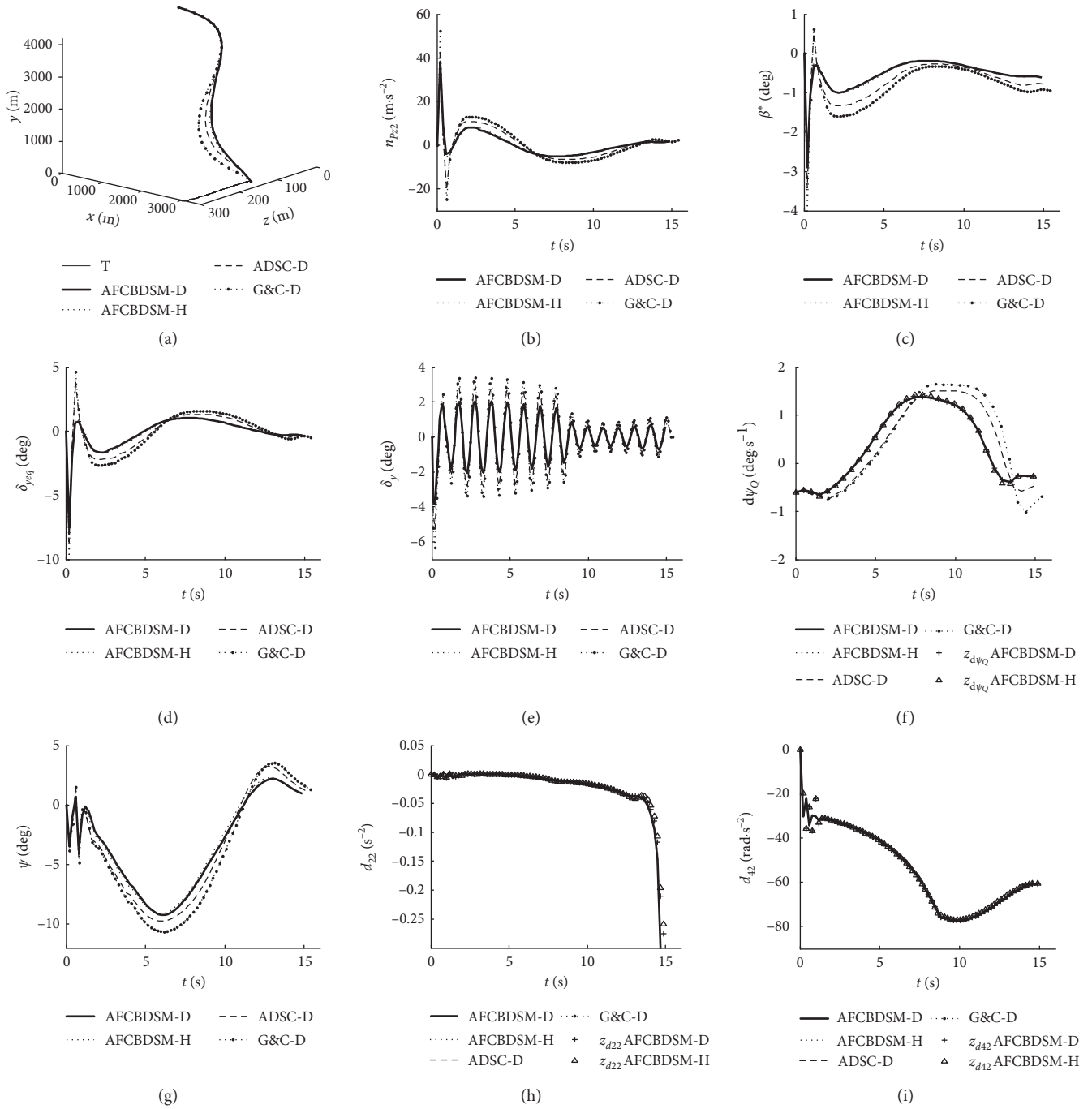
FIGURE 3: Experimental curves of operating condition 1. (a) Trajectory of projectile and target. (b) Normal overload. (c) Quasi-attack angle. (d) Equal pitch canard angle. (e) Pitch canard angle. (f) LOS inclination angle rate. (g) Pitch angle. (h) $z_{d_{21}}$ and disturbance d_{21}. (i) $z_{d_{41}}$ and disturbance d_{41}.

TABLE 6: Experimental results of operating condition 1.

Method	θ_Q error (deg)	ψ_Q error (deg)	Miss distance (m)	Hit time (s)
AFCBDSM-D	0.09	0.07	0.15	14.87
AFCBDSM-H	0.13	0.12	0.18	14.90
ADSC-D	0.27	0.24	0.31	15.12
G&C-D	0.38	0.35	0.53	15.34

Figure 4: Experimental curves of operating condition 2. (a) Trajectory of projectile and target. (b) Lateral overload. (c) Quasi sideslip angle. (d) Equal yaw canard angle. (e) Yaw canard angle. (f) LOS azimuth angle rate. (g) Yaw angle. (h) $z_{d_{22}}$ and disturbance d_{22}. (i) $z_{d_{42}}$ and disturbance d_{42}.

Table 7: Experimental results of operating condition 2.

Method	θ_Q error (deg)	ψ_Q error (deg)	Miss distance (m)	Hit time (s)
AFCBDSM-D	0.11	0.09	0.17	14.89
AFCBDSM-H	0.14	0.12	0.20	14.93
ADSC-D	0.32	0.28	0.34	15.17
G&C -D	0.41	0.37	0.58	15.41

the guided projectile while attacking a square wave maneuvering target. And from Table 7, the AFCBDSM optimized miss distance, hit time, and LOS angle tracking errors, which was conducive to fine adjustments of the guided projectile in the terminal guidance process.

The trend of lateral overload is demonstrated in Figure 4(b). With fixed gain parameters, ADSC relied only on the dynamic surface sliding mode to stabilize the system, which caused the initial value to change greatly, the peak value to become large, and the terminal convergence rate to be slow. However, the AFCBDSM effectively weakened the chatter of the block dynamic surface sliding modes by the adaptive adjustment of the fuzzy parameters and the terminal convergence rate was faster, which demonstrates the robustness of the system.

According to Figure 4(c), the change in β^* was basically consistent with lateral overload, which confirms the correctness of Assumption 2. Compared with ADSC and G&C, the projectile had a smaller peak and slower change of β^* under the control of the AFCBDSM through the ESO and adaptive fuzzy systems, which could adapt to various unknown disturbances.

As can be seen from Figure 4(d), ADSC and G&C easily exhibited saturation of the canard deflection, owing to it did not account for the nonlinear saturation of the canard deflection. Moreover, under the internal and external disturbances of the system, δ_{yeq} varied widely and rapidly, which usually wastes precious energy and can even cause irreversible damage to canard. However, the AFCBDSM could avoid this, which verified the effectiveness of the adaptive Nussbaum gain function for handling control saturation of the actuator.

As shown in Figure 4(e), the yaw channel of the canard could meet the requirements of the actual canard deflection in the switching frequency and amplitude. Unlike ADSC and G&C, the AFCBDSM further optimized the range and mutation of δ_y.

From the analysis of Figure 4(f), the channel coupling effect acting on the yaw channel was greater than that acting on the pitch channel, which resulted in a slower convergence rate of $\dot{\psi}_Q$ than that of $\dot{\theta}_Q$. ADSC and G&C were more affected by disturbances due to the ineffective processing of disturbances and chatter, and it even failed to reach convergence at hitting time. Whereas, with the AFCBDSM, ψ_Q and $\dot{\psi}_Q$ converged to zero after 14 s under the control of the designed ESO and adaptive fuzzy systems, which indicated $\mathbf{s}_2$ could converge in finite time.

Because of the influence of channel coupling, the ESO could not completely observe the uncertain disturbance d_{42} initially. However, it subsequently entered a continuous smooth state quickly. From another perspective, the yaw channel of the turntable possessed good tracking characteristics.

Figures 4(f), 4(h), and 4(i) showed that the designed ESO possessed good observational properties and robustness. Even with fast variations and a wide range of disturbances, the ESO could observe the LOS azimuth angle rate and disturbances quickly and accurately, which provided necessary feedback information.

6. Conclusion

Aiming at the terminal guidance stage for hitting coastal maneuvering targets, the AFCBDSM was designed for large caliber naval gun-guided projectiles. It was theoretically proven and demonstrated with HILS experiments that the AFCBDSM exhibited well-terminal guidance performances while hitting a target with different maneuvering forms. The results are highlighted as follows:

(1) With multiple constraints and various disturbances comprehensively considered, the IGC strict feedback cascade model for rolling naval gun-guided projectile was constructed

(2) The switching chatter of the block dynamic surface sliding mode was effectively weakened by the adaptive fuzzy system

(3) The finite time convergence of LOS angle tracking errors, LOS angle rate, and UUB of the closed-loop system were strictly proven

(4) The effectiveness and feasibility of the AFCBDSM were validated through the designed HILS system, which possesses certain theoretical and engineering values

Data Availability

The data used to support the findings of this study are available from the corresponding author upon request.

Conflicts of Interest

The authors declare no potential conflicts of interest with respect to the research, authorship, and/or publication of this article.

Acknowledgments

References

[1] P. Kishore and O. Ernest, "Evaluation of two guidance laws for controlling the impact flight path angle of a naval gun launched spinning projectile," in *Proceedings of AIAA Guidance, Navigation, and Control Conference and Exhibit*, Keystone, CO, USA, August 2006.

[2] A. Zhurbal and M. Idan, "Effect of estimation on the performance of an integrated missile guidance and control system," *IEEE Transactions on Aerospace and Electronic Systems*, vol. 47, no. 4, pp. 2690–2708, 2011.

[3] S. Jiang, F. Q. Tian, S. Y. Sun et al., "Fuzzy adaptive dynamic surface terminal guidance law considering autopilot and impact angle constraints," *System Engineering and Electronics*, vol. 41, no. 2, pp. 389–401, 2019.

[4] K. W. Lee and S. N. Singh, "Longitudinal nonlinear adaptive autopilot design for missiles with control constraint," *Proceedings of the Institution of Mechanical Engineers, Part G:*

Journal of Aerospace Engineering, vol. 232, no. 9, pp. 1655–1670, 2018.

[5] L. Wang, W. H. Zhang, D. H. Wang, K. Peng, and H. Yang, "Command filtered back-stepping missile integrated guidance and autopilot based on extended state observer," *Advances in Mechanical Engineering*, vol. 9, no. 11, pp. 1–13, 2017.

[6] D. Williams, J. Richman, and B. Friedland, "Design of an integrated strapdown guidance and control system for a tactical missile," in *Proceedings of AIAA Guidance and Control Conference*, pp. 57–66, Gatlinburg, TX, USA, August 1983.

[7] J. Yang, X. G. Wang, Z. Y. Wang et al., "Sliding-mode-observer-based robust variable structure control for integrated autopilot-guidance," *Acta Armamentarii*, vol. 38, no. 2, pp. 246–253, 2017.

[8] C. Wen, J. Zhou, Z. Liu, and H. Su, "Robust adaptive control of uncertain nonlinear systems in the presence of input saturation and external disturbance," *IEEE Transactions on Automatic Control*, vol. 56, no. 7, pp. 1672–1678, 2011.

[9] S. H. Seyedipour, M. Fathi Jegarkandi, and S. Shamaghdari, "Nonlinear integrated guidance and control based on adaptive backstepping scheme," *Aircraft Engineering and Aerospace Technology*, vol. 89, no. 3, pp. 415–424, 2017.

[10] X. L. Shao and H. L. Wang, "Back-stepping active disturbance rejection control design for integrated missile guidance and control system via reduced-order ESO," *Isa Transactions*, vol. 57, no. 4, pp. 10–22, 2015.

[11] Y. B. Shtessel and C. H. Tournes, "Integrated higher-order sliding mode guidance and autopilot for dual-control missiles," *Journal of Guidance Control Dynamics*, vol. 32, no. 1, pp. 79–94, 2012.

[12] P. Wu and M. Yang, "Integrated guidance and control design for missile with terminal impact angle constraint based on sliding mode control," *Journal of Systems Engineering and Electronics*, vol. 21, no. 4, pp. 623–628, 2010.

[13] S. R. Kumar, S. Rao, and D. Ghose, "Nonsingular terminal sliding mode guidance with impact angle constraints," *Journal of Guidance, Control, and Dynamics*, vol. 37, no. 4, pp. 1114–1130, 2014.

[14] C. Guo and X.-G. Liang, "Integrated guidance and control based on block backstepping sliding mode and dynamic control allocation," *Proceedings of the Institution of Mechanical Engineers, Part G: Journal of Aerospace Engineering*, vol. 229, no. 9, pp. 1559–1574, 2015.

[15] M. Ran, Q. Wang, D. Hou, and C. Dong, "Backstepping design of missile guidance and control based on adaptive fuzzy sliding mode control," *Chinese Journal of Aeronautics*, vol. 27, no. 3, pp. 634–642, 2014.

[16] J. Han, "From PID to active disturbance rejection control," *IEEE Transactions on Industrial Electronics*, vol. 56, no. 3, pp. 900–906, 2009.

[17] Z. P. Han, *Exterior Ballistics of Projectiles and Rockets*, Beijing Institute of Technology Press, Beijing, China, 2014.

[18] J. Chang, Z. Guo, J. Cieslak, and W. Chen, "Integrated guidance and control design for the hypersonic interceptor based on adaptive incremental backstepping technique," *Aerospace Science and Technology*, vol. 89, pp. 318–332, 2019.

[19] S. M. He, W. Wang, and J. Wang, "Adaptive backstepping impact angle control with autopilot dynamics and acceleration saturation consideration," *International Journal of Robust and Nonlinear Control*, vol. 27, no. 17, pp. 3777–3794, 2017.

[20] Y. Feng, X. Yu, and Z. Man, "Non-singular terminal sliding mode control of rigid manipulators," *Automatica*, vol. 38, no. 12, pp. 2159–2167, 2002.

[21] R. D. Nussbaum, "Some remarks on a conjecture in parameter adaptive control," *Systems & Control Letters*, vol. 3, no. 5, pp. 243–246, 1983.

[22] Y. Li, S. Tong, and T. Li, "Direct adaptive fuzzy backstepping control of uncertain nonlinear systems in the presence of input saturation," *Neural Computing and Applications*, vol. 23, no. 5, pp. 1207–1216, 2013.

[23] M.-Z. Hou and G.-R. Duan, "Adaptive dynamic surface control for integrated missile guidance and autopilot," *International Journal of Automation and Computing*, vol. 8, no. 1, pp. 122–127, 2011.

[24] T. Yamasaki, S. N. Balarishnan, H. Takano et al., "Second order sliding mode-based intercept guidance with uncertainty and disturbance compensation," in *Proceedings of the AIAA Guidance, Navigation, and Control (GNC) Conference*, vol. 39, no. 5, pp. 1–17, Boston, MA, USA, August 2013.

[25] M. Hou, X. Liang, and G. Duan, "Adaptive block dynamic surface control for integrated missile guidance and autopilot," *Chinese Journal of Aeronautics*, vol. 26, no. 3, pp. 741–750, 2013.